CHAPTER 5

RESULTS AND ANALYSIS

5.1 Introduction

This chapter discusses the experimental results and simulation analysis. The first part discusses the physical observations of the bubble flow and the bubble flow regime map which is obtained by applying the experimental conditions on the ECT sensor (i.e. co-current bubble column). It illustrates the experimental observations of bubbles characteristics and its flow regime classification. It also includes ECT measurement, calibration and normalisation for air-water two-phase flow. The simulation results of ECT sensor by using COMSOL software is also studied and compared with the experimental measurements. The second part covers the void fraction estimation from the Delta-P and photographic technique and also compares its results with the drift-flux model. The estimation of void fraction from ECT measurements and its comparison with Delta-P and photographic technique is also presented.

5.2 Analysis of Bubble Flow Regime

The aim of two-phase flow research emphasized the prediction of flow regimes so that the basic characteristics of those flow regimes can be established. Thus one of the most important aspects of this work was the determination of the bubble flow regime. The detailed study on the behaviour of the bubble flow regime and its different types studied on the vertical two-phase flow test setup along with the photographic views and flow map are discussed in the following sections.

5.2.1 Visual Observations

5.2.1.1 Discrete Bubble Flow

This flow regime obtained under *low air-water* superficial velocities (U_{sg} = 0.00874 - 0.0218 m/sec and U_{sl} = 0.00425 – 0.0131 m/sec). Because of low gas velocity, the bubbles formed initially were of small size, spherical in shape and uniformly distributed within the column. The size of the bubbles also depends on the gas distributor which possesses small holes and the bubble frequency is low, less chance for the bubbles to coalesce. It has also been observed that at low liquid velocity, the turbulence is small. Figure 5.1 (a) shows the physical image of the flow.

5.2.1.2 Dispersed Bubble Flow

This flow pattern is encountered at *high water* and from *low to intermediate air* superficial velocities (U_{sg} = 0.0109 – 0.024 m/sec and U_{sl} = 0.0262 – 0.0349 m/sec). The bubbles in this regime, however, are smaller and more uniform and also no bubble to bubble interaction existed because of high liquid rate turbulence. Figure 5.1 (b) shows the physical image of the dispersed bubble flow.

5.2.1.3 Coalesced Bubble Flow

This flow regime generates at *low water* and *intermediate air* superficial velocities (U_{sg} = 0.022 – 0.0305 m/sec and U_{sl} = 0.00425 – 0.0218 m/sec). It is confined to a very narrow gas velocity range due to small diameter column used in this study. Figure 5.1 (c) shows the physical representation of the coalesced bubble flow.

The behaviour of gas bubbles in discrete and dispersed bubble flow regime may be characterised as the homogenous regime. While in the coalesced bubble flow regime, the size of gas bubbles increases as the gas velocity has increased which cause bubbles to coalesce and classify them as more towards the heterogeneous flow.

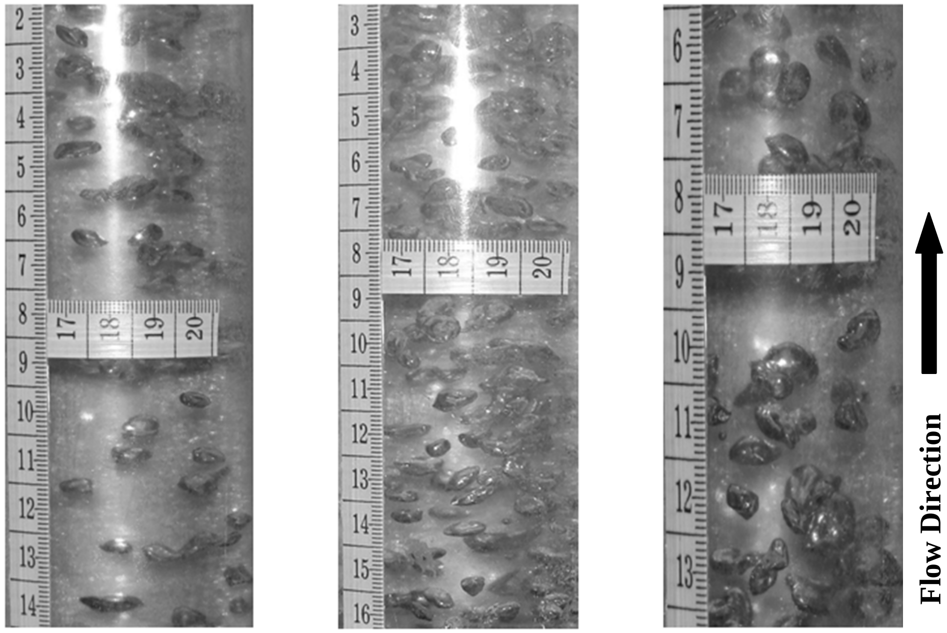

(a) (b) (c)

Figure 5.1: Bubble Flow Regime for Air-Water Mixture: (a) Discrete Bubble Flow (b) Dispersed Bubble Flow and (c) Coalesced Bubble Flow.

Table 5.1 reveals the detailed specifications of the above mentioned flow regimes. It consists of superficial air velocity, superficial liquid velocity, Reynolds number for air and Reynolds number for water for each type of bubble flow regime as shown in Figure 5.1.

Table 5.1: Physical Properties for Different Kinds of Bubble Flow Regime

Type of Bubble Flow	U_{sg} **(m/sec)**	U_{sl} **(m/sec)**	Re_{sg}	Re_{sl}
Discrete	0.0153	0.0131	50.5	854.56
Dispersed	0.024	0.0305	76.97	1499.9
Coalesced	0.0218	0.0131	43.23	1080.5

5.2.2 Bubble Flow Regime Map for Air-Water Column

5.2.2.1 Experimental Results

The flow visual observation is the most common practice to identify the flow regimes beside other techniques. It is a physical study of flow characteristics and its corresponding graphical interpretation on a flow pattern map. The bubble flow regime boundaries as mentioned in Figure 5.2 is summarised in Table 5.2. Figure 5.2 presents the bubble flow regime map for the 49.3 mm inner diameter vertical upflow condition employing air and deionised water as working fluid. It is obtained by plotting the gas superficial velocity, $U_{sg}=Q_g/A$ (m/sec) against the liquid superficial velocity, $U_{sl}=Q_w/A$ (m/sec). The nominal area of the pipe, A, is calculated as 0.00191m^2 using the pipe diameter as 0.0493 m. Q_g (m^3/sec) is the gas volumetric flow rate at the operating condition of temperature and pressure while the Q_w (m^3/sec) is the liquid volumetric flow rate. The map is obtained for air superficial velocity range of 0.00218 – 0.03 m/sec and water superficial velocity range of 0.00425- 0.034 m/sec.

Table 5.2: Bubble Flow Regime Boundaries for Air-Water System with D = 0.0493 m

Discrete/Dispersed		**Discrete/Coalesced**	
U_{sg} (m/sec)	**U_{sl} (m/sec)**	**U_{sg} (m/sec)**	**U_{sl} (m/sec)**
0.00874	0.022	0.0153	0.00425
0.0109	0.022	0.0158	0.00874
0.0131	0.022	0.0167	0.0131
0.0153	0.0234	0.0154	0.0174
0.0174	0.0234	0.0142	0.022
0.0196	0.0234	0.0146	0.0262
0.022	0.0262	0.0234	0.0305
0.0234	0.0262	0.0305	0.034

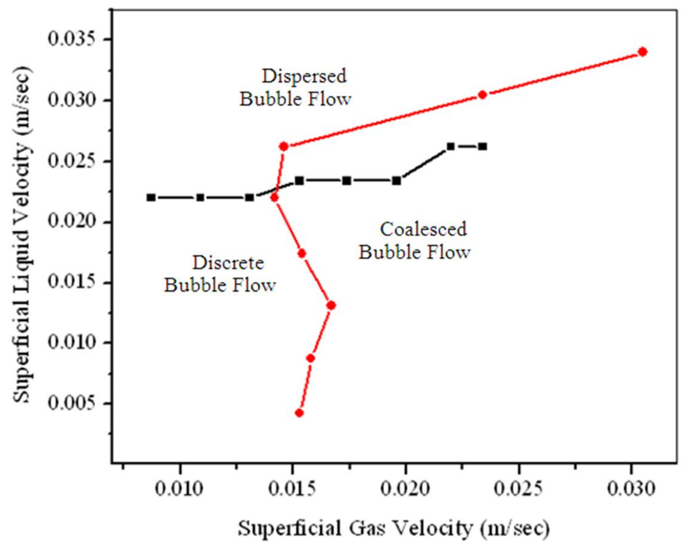

Figure 5.2: Bubble Flow Regime Map for Vertical Air-Water Co-Current Column with D = 0.0493 m and H = 0.41 m, Multiple Orifice Plate Containing 1 mm Circular Holes.

In the above figure, the flow patterns observed namely are; discrete, dispersed and coalesced bubble flow regimes are shown at their respective locations. It can be seen that discrete bubble flow regime predominates at low air and water velocities, while the dispersed bubble flow regime observed at higher liquid velocities and due to liquid turbulence bubbles flowed upward without any interaction with one another. Both discrete and dispersed bubble flow regimes can be categorized by small bubbles having a uniform size. The coalesced bubble flow regime in Figure 5.2 emerges for a very narrow gas velocity range due to small diameter column used in this study.

5.2.2.2 Comparison with the Precedent Study

Figure 5.3 is a graphical comparison between the bubble flow regime map of the current study with the flow pattern map of the previous research study as mentioned in section *2.7.2*. In this regard, the model of J.P.Zhang et al. (1997) is compared as the flow rates of this study are considerably found closest with the current ranges of flow rates [45]. The remaining models of section *2.7.2* are for higher range of flow rates which is not appropriate for comparison with the current experimental study.

This comparison determines the validity of the current flow pattern map with the experimental flow regimes. It can also be seen from the plot that both the models follow the same trend. The bubble flow regime map in Figure 5.3 shows a transition from discrete to dispersed and then to coalesced bubble flow.

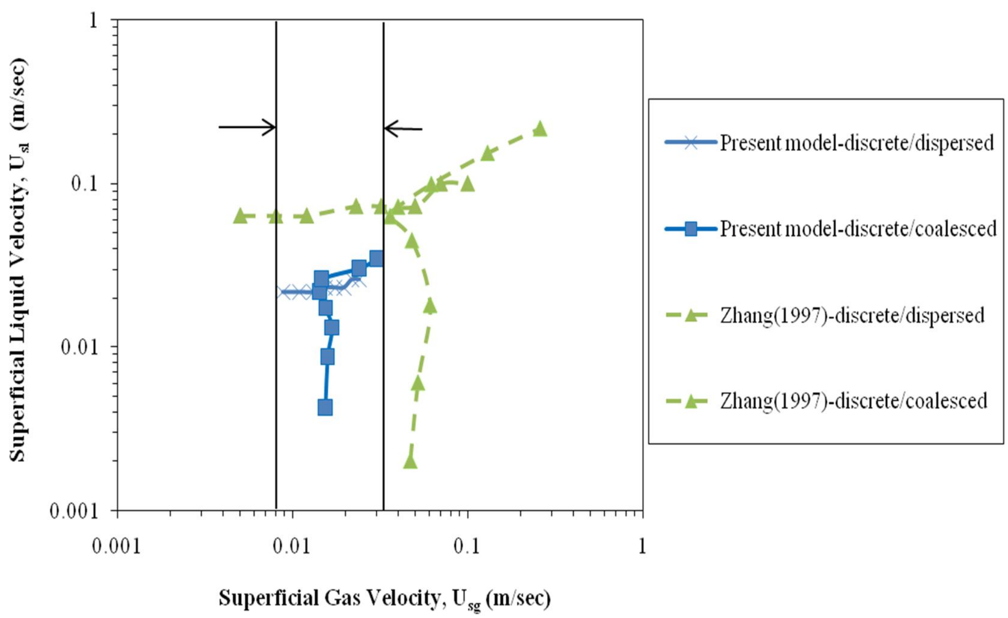

Figure 5.3: Comparison of Co-Current Two-Phase Vertical Bubble Flow Regime Map with Previous Studies (Data for Air-Water System, θ = 90°, D = 4.93 cm).

5.2.3 Bubbles Characteristics

A basic parameter in two-phase gas-liquid flow is the size of the bubbles. The size of bubbles is as important as the void fraction or holdup. The estimation method of bubble size was measured by taking photographs and then compared empirically with previous published correlations. By using the correlations to measure the bubble size, it diminishes time to measure other parameters and also their experimental errors. The measurements were performed in a circular cross-section which is made from Perspex, as this was convenient for visual and photographic observations.

Bubble diameters have been measured as a function of the gas superficial velocity in air-water system. However, the average bubble size in a bubble column has found to be affected by gas velocity, column and orifice diameter, surface tension, density and kinematic viscosity of the liquid [85]. Figure 5.4 illustrates that the average bubble diameter varies with superficial velocities of air and water at 20 ± 2 °C in a 49.3 mm diameter pipe. For a given liquid superficial velocity, the diameter of bubbles initially decreases rapidly and then decreases gradually with further increase in superficial gas velocity.

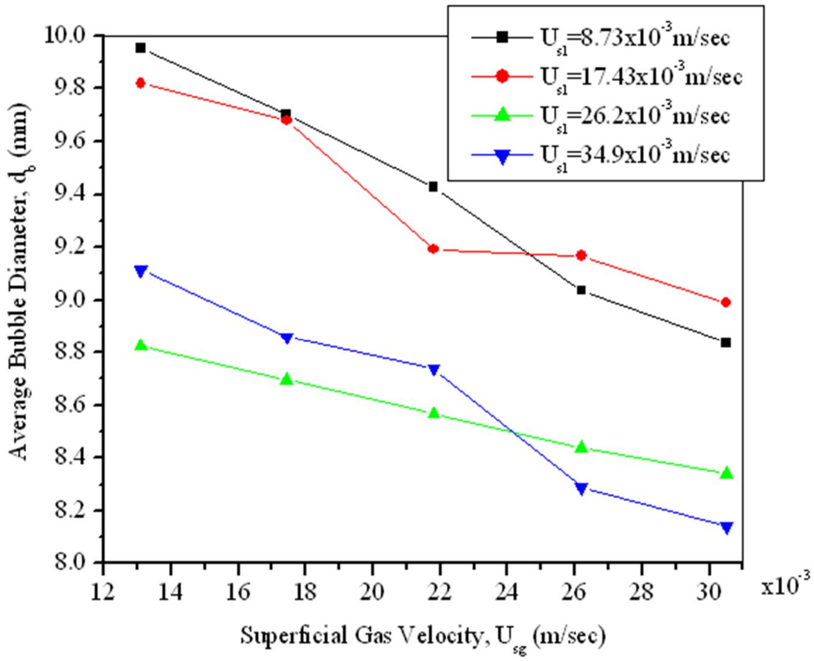

Figure 5.4: Average Bubble Diameter as a Function of Superficial Gas Velocity at Different Liquid Flow Rate.

According to Jamialahmadi (1992), the bubble size is a strong function of the orifice diameter in the bubbly flow regime [86]. The bubble size in the range of this study can be empirically estimated using equations (5-1) and (5-2) [85], [87]. Based on the experimental data, Akita and Yoshida (1974) investigated a decrease in bubble size with increasing gas flow rate and proposed the following correlation for estimation of bubble size as a function of the superficial gas velocity and the physical properties of the system;

$$d_b = 26D_i\left(\frac{D_i^2 g\rho_l}{\sigma}\right)^{-0.5}\left(\frac{gD_i^3}{v_L^2}\right)^{-0.12}\left(\frac{U_{sg}}{\sqrt{gD_i}}\right)^{-0.12} \tag{5-1}$$

$$\frac{g\rho_l d_b^2}{\sigma_L} = 38.8\left(\frac{U_{sg}\mu_l}{\sigma_L}\right)^{-0.04}\left(\frac{\rho_l\sigma_L^3}{g\mu_L^4}\right)^{-0.12}\left(\frac{\rho_l}{\rho_g}\right)^{-0.22} \tag{5-2}$$

where, d_b is the average bubble size; D_i is the column inner diameter; ρ_l is liquid density; σ_L is surface tension; μ_L is liquid viscosity; υ_L is liquid kinematic viscosity; U_{sg} is the superficial gas velocity and g is the gravitational constant.

The average bubble size estimated by equations (5-1) and (5-2) are shown in Figure 5.5. This figure clearly demonstrates that by using the above mentioned correlations, there is a gradual reduction in bubble size with increasing superficial gas velocity which is in agreement with the experimental trend. The maximum bubble size for this experimental setup of air-water system was 10 mm with the majority of bubbles being between 8 to 9.95 mm at U_{sg} = 1.31 to 3.05 cm/sec. The bubble sizes measured empirically are in good agreement with the photographic scaled observations. The application of *2^nd^* order polynomial regression in Figure 5.5 also validates the data by showing the correlation coefficient (R^2) close to 1.

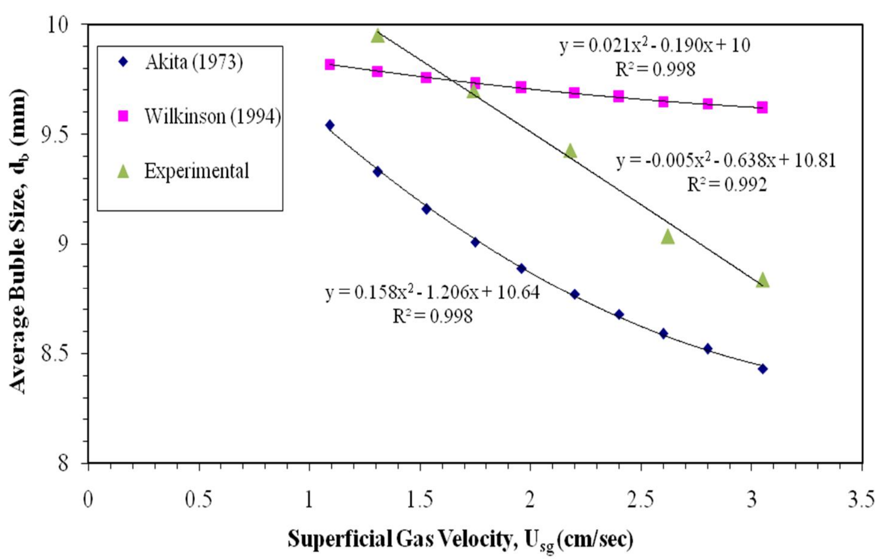

Figure 5.5: Comparison between Measured Data and Values Calculated Using the Equations (5-1) and (5-2).

5.3 ECT Measurement

A number of different measurement protocols can be used for the capacitance measurement in an ECT system but the mostly used measurement protocol is where capacitances are measured between single pair of electrodes. During a measurement period, each electrode in an ECT sensor is energised by applying the excitation voltage signal. The remaining detector electrodes are kept at zero potential and the currents which flow into these electrodes are measured. For this study, 12 electrodes sensor has been used, first electrode 1 is excited and electrodes 2-12 kept at zero potential. Next, electrode 2 is excited and electrode 3-12 kept at zero potential. This continues until electrode 11 is excited and obtained 11-12 as last measurement. Considering this measurement principle, the number of measurements generates for the 12-electrode sensor is 66 (equation defined in section *3.2.1*).

5.3.1 Calibration of an ECT Sensor

The calibration of an ECT sensor is very important and necessary step in order to ensure the reliability of capturing the images accurately. When a mixture of two dielectric materials has to be imaged then ECT systems are preferred to be calibrated. ECT sensors are calibrated by measuring two reference sets of inter-electrode capacitances, one is for a lower permittivity i.e. C_l, followed by a higher permittivity material i.e. C_h. In our case, an ECT sensor is calibrated using two different materials for example, air and deionized water. They have different dielectric properties, particularly the permittivity value. So for this case, the sensor is first measured empty i.e. using air having the permittivity equals to one and also it gives the value of lower capacitance C_l , and then it is completely filled with deionized water having the higher permittivity equals to 80 that will gives the values for higher capacitance $C_{h.}$

The calibration has been done using the 12-electrode ECT sensor whose results were analysed on the ECT software that was provided with the data acquisition system. As a first step, the sensor has been filled with air (empty) to perform the low calibration. The ECT software was used for online measurements and then for visualising and further analysis of the data can be done by using other software.

The raw voltage and capacitance measurements further exported on MS Excel to manipulate the data. The second step was to perform the high calibration by filling the whole sensor with the deionised water

Figure 5.6 shows that the calibration data retrieved from the acquisition system is based on average measurements and has been converted to the following tomogram images. The low calibration data (when the sensor filled with air) indicates a blue tomogram and high calibration data (when the sensor filled with deionised water) indicates a red tomogram image. The tomogram images of the calibration are based on the normalised values from 0 to1. The colour-scale for ECT is used to display the variation in permittivity between 0 to 1, indicating 0 as low permittivity and 1 as high permittivity.

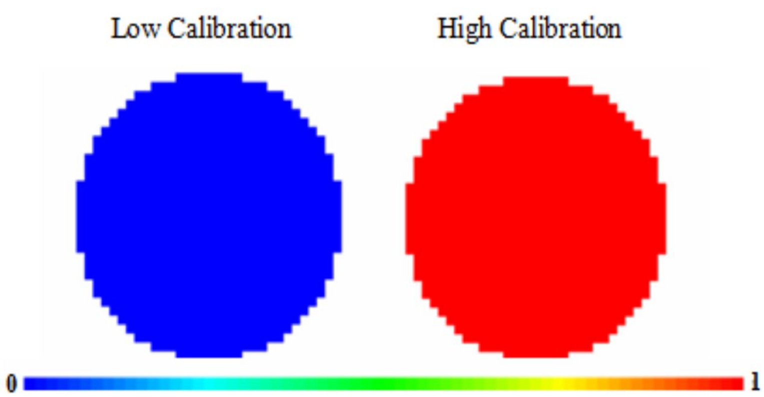

Figure 5.6: Low *vs.* High Calibration Images.

Figure 5.7 illustrates the voltage line graph in which air has high voltage values while deionised water indicates the low voltage values. In the following graph, X-axis indicates the number of electrode pairs and Y-axis indicates the voltage value. Comparing both line graphs, low calibration shows slightly higher voltage value. This is expected because water (high calibration) has permittivity of 80 while air (low calibration) has permittivity of around 1. This line graph also shows a good symmetrical curve between air and water measurements, indicating a measurement span and the sensitivity of the sensor.

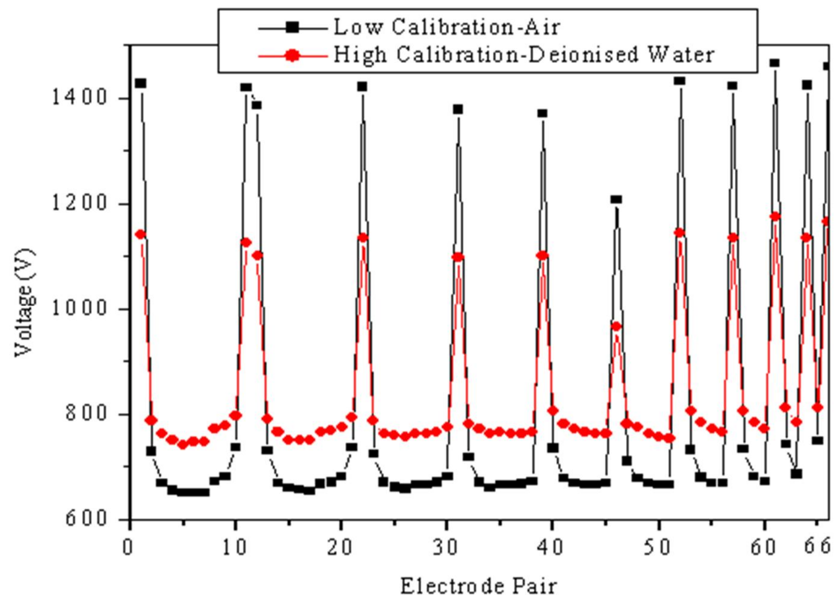

Figure 5.7: Low *vs.* High Calibration Line Graph.

5.3.2 Online Measurement for Two-Phase Flow

Once a good calibration data has been obtained then the acquisition unit and ECT sensor has been set for the online measurements of air and deionised water. The ECT sensor was then connected to the piping loop by using connectors. Two types of experiments being performed on the test rig are:

i. *Static*

ii. *Dynamic*

During each test, the ECT flow images were displayed on the computer screen in a real time and also recorded on its hard disk.

5.3.2.1 Static Measurements

In the static test, the sensor was placed vertically during the measurements. This test was conducted between the tap water and deionised water with different water distributions within the sensor. The results for this test are given below in Table 5.3 and Figure 5.8 and 5.9.

Table 5.3: Static Test with Tap Water and Deionised Water

Static test with Tap Water ***(σ= 69.2 μS/cm)***	***Static test with Deionised Water*** ***(σ= 0.35 μS/cm)***
Tomogram Images (For Frame 3)	
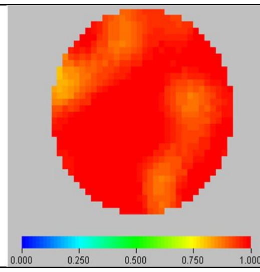	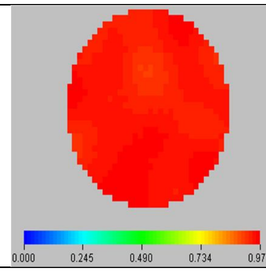
With Metallic Rod in the Sensing Domain	
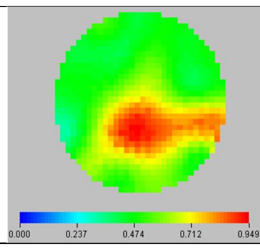	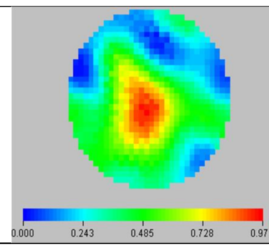
With PVC Rod in the Sensing Domain	
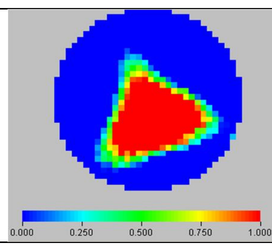	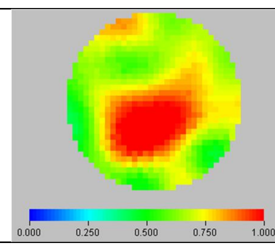

(a) Static Test with Tap Water

After a good calibration data has been achieved then the sensor was completely filled with tap water having conductivity of 69.2 micro Siemens per centimetre (μS/cm). Table 5.3 indicates the result for tap water in comparison with deionised water. Initially, it shows only the tomogram images for the tap water filled in the sensor, secondly it displays the images for two different types of rods inserted in the column; one is PVC rod and another is metallic rod.

(b) Static Test with Deionised Water

The static test with deionised water also conducted the same way as with tap water. Initially the sensor was calibrated with lower and higher permittivity material; then it was completely filled with the deionised water having conductivity of 0.35 micro Siemens per centimetre (μS/cm) to perform the online measurements. Table 5.3 signifies the tomogram images for this test along with the tap water.

From the figure above in the Table 5.3, the conductivity effect can be clearly seen from the tomogram images. The metal rod from the conductive element has shown completely different image in comparison with the PVC rod. As known, ECT sensor is the most suitable for non-conductive element. Thus, if any of the conductive elements are flowing through the pipe, it will influence the type of tomogram itself. Figure 5.8 and 5.9 below demonstrates the results for raw capacitance and voltages between tap water and deionised water obtained from the static test.

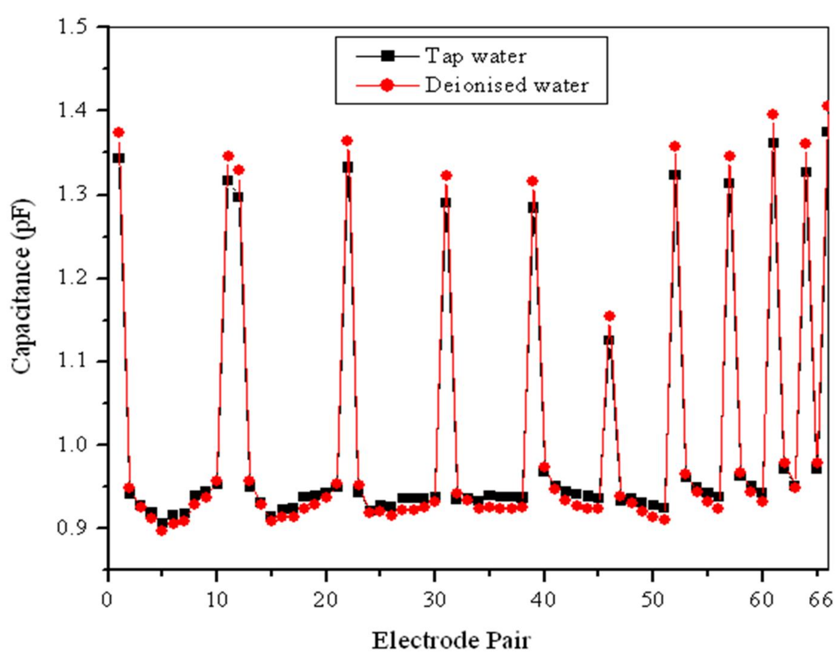

Figure 5.8: Comparison of Raw Capacitance between Tap and Deionised Water.

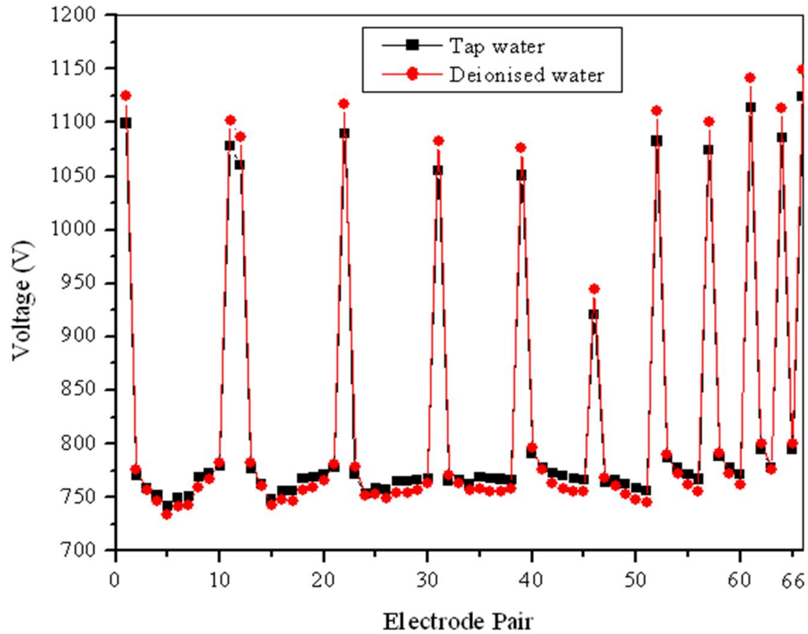

Figure 5.9: Comparison of Raw Voltages between Tap and Deionised Water.

5.3.2.2 Dynamic Measurements

For dynamic measurements, the test section was pressurized with air and deionized water by opening the control valves. Different tests were then performed in order to get the two-phase flow measurements by varying the air and water flow rates. As a result, distinctive bubble flow regimes were observed as discussed in section *5.2*. Figure 5.10 shows the typical tomographic images to the corresponding flow rates. The ECT images were produced using the linear back-projection (LBP) reconstruction algorithm. This offer fast processing time in comparison with other algorithms; however, it does produce qualitative, rather than quantitative, images. The images represent the cross-sectional phase distribution inside the sensor.

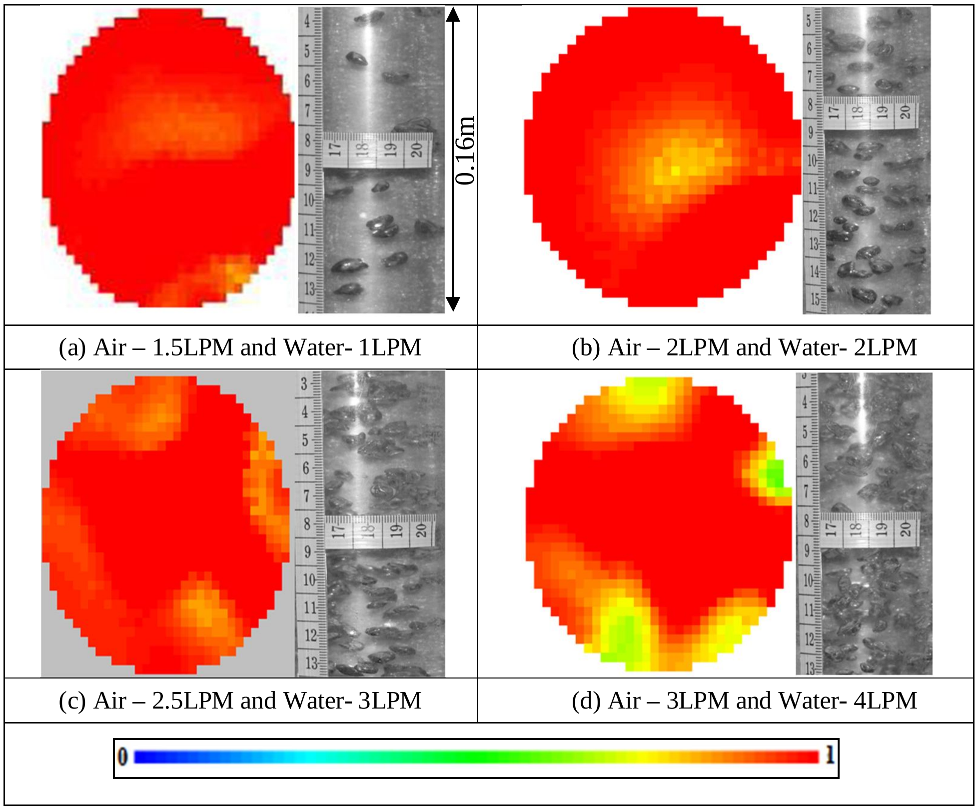

(a) Air – 1.5LPM and Water- 1LPM

(b) Air – 2LPM and Water- 2LPM

(c) Air – 2.5LPM and Water- 3LPM

(d) Air – 3LPM and Water- 4LPM

Figure 5.10: Tomographic Images and Flow Pattern.

5.3.3 Normalisation of Measurements

The number of sensor electrodes that can be used depends on the range of values of inter-electrode capacitances and the upper and lower measurement limits of the capacitance measurement circuit. The capacitance values when the sensor contains air are referred to as "standing capacitances". Sequential electrodes are called as "adjacent electrodes", and have the largest standing capacitance, while diagonally opposing electrodes have the smallest capacitances. Because of this wide range of capacitances, they are normalised normally so that they can lie within the certain range of values. The inter-electrode capacitances measured at low permittivity (C_l) are assigned as "0" while the inter-electrode capacitances measured at higher permittivity (C_h) are assigned the value as "1" and are defined by the equation as discussed in section *3.2.4.1*.

To check the validity of the above statement the following procedure was followed. The capacitance measurements obtained by using the air served as low permittivity values while the capacitance measurements obtained by using the water served as the high permittivity values. These capacitance measurements were then normalised in order to withstand the values within the permissible range.

Figure 5.11 shows the comparison of normalised inter-electrode capacitances obtained from Parallel model for air-water two-phase flow, when the air flow rate was kept at 2.75 LPM and the liquid flow rate constant at 1 LPM. The normalised capacitance for this particular case acquire in the range of 0.65 ≥ C_n ≥ 0.68 which is under the range of 0 ≥ C_n ≥ 1.

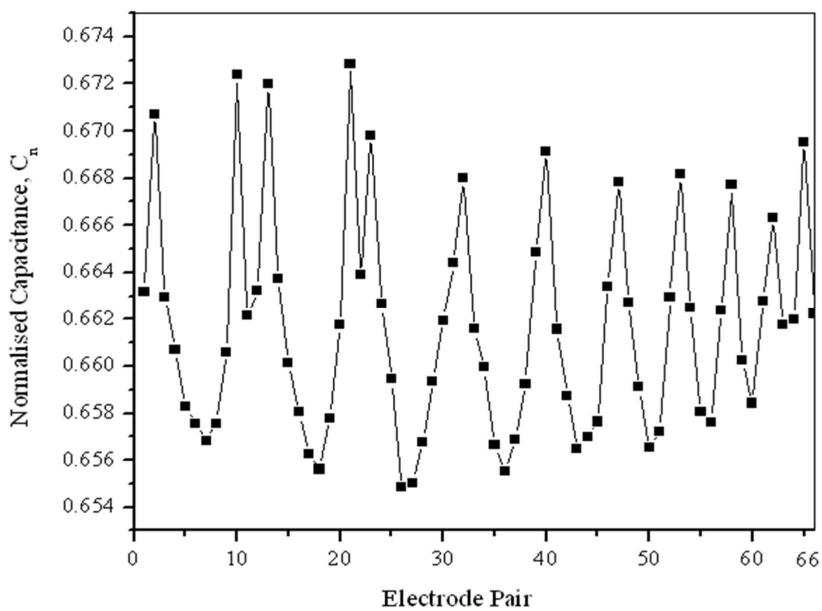

Figure 5.11: Normalised Inter-electrode Capacitance for Q_g = 2.75 LPM and Q_w = 1 LPM.

5.4 Modelling of ECT Sensor

5.4.1 Without Radial Guards

COMSOL utilized the approach of finite element method (FEM) to calculate the potential distribution. It is used in sensor performance evaluation. Through simulation comparison of full pipe of Perspex and an empty pipe, we get the distribution of electric sensitive potential and media distribution on the sensitive field. The sensor simulation details are shown in Table 5.4.

Table 5.4: ECT Sensor Details

ECT Sensor	Specifications
No. of electrodes	12
Inner / outer pipe diameter	49.3/65.2 mm
Earth screen diameter	120 mm
Thickness of electrodes	1 mm
Guards between electrodes	2 mm
Permittivity of pipe wall	$\varepsilon_r = 3$
Permittivity of Water	$\varepsilon_W = 80$
Permittivity of Air	$\varepsilon_A = 1.0$
Excitation Voltage	$\varphi = 15V$

Based on the above mentioned specifications, the simulation results for the air (empty) filled and the water (full) filled sensor is shown in Figure 5.12 (a) and (b). It shows the node potential distribution when one electrode is excited with a potential of 15V and the others are kept at ground potential. The blue area represents the region of the pipe without the potential i.e. $\varphi = 0V$ but the coloured area represents the region of the pipe with different node potential i.e. the domain of electrode can be sensitive. The nearer distance to the initialized electrode will have a higher potential distribution. The standing capacitances without guards are much more sensitive with respect to the distance between the electrodes and the screen.

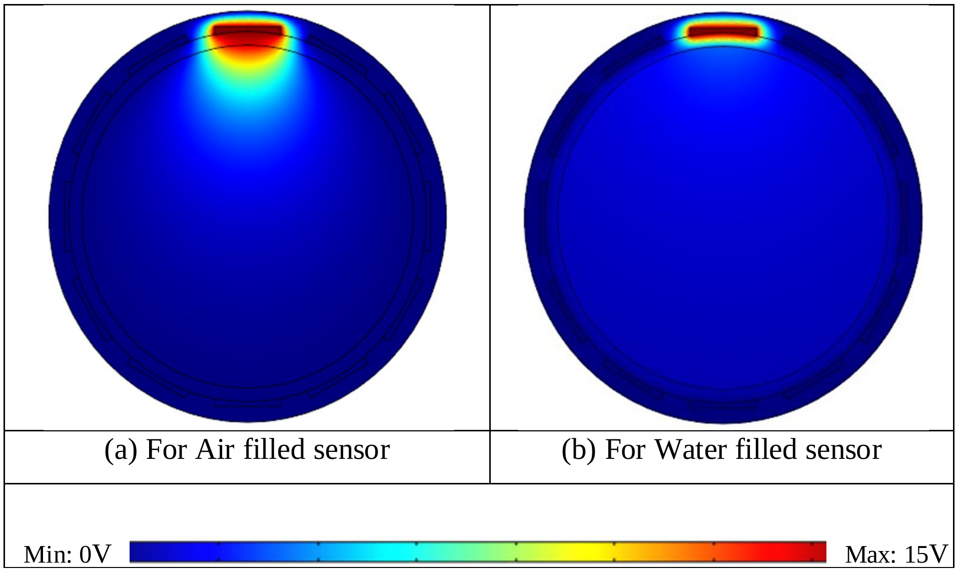

(a) For Air filled sensor | (b) For Water filled sensor

Figure 5.12: Electrical Potential Distribution for (a) Air and (b) Water in *2D*.

The excitation method for ECT sensor is based on single electrode excitation to measure mutual capacitances. Figure 5.13 indicates that the equipotential lines are concentrated in the area near the electrodes with high voltage i.e. the electric field intensity near the electrode is much higher than in the other area.

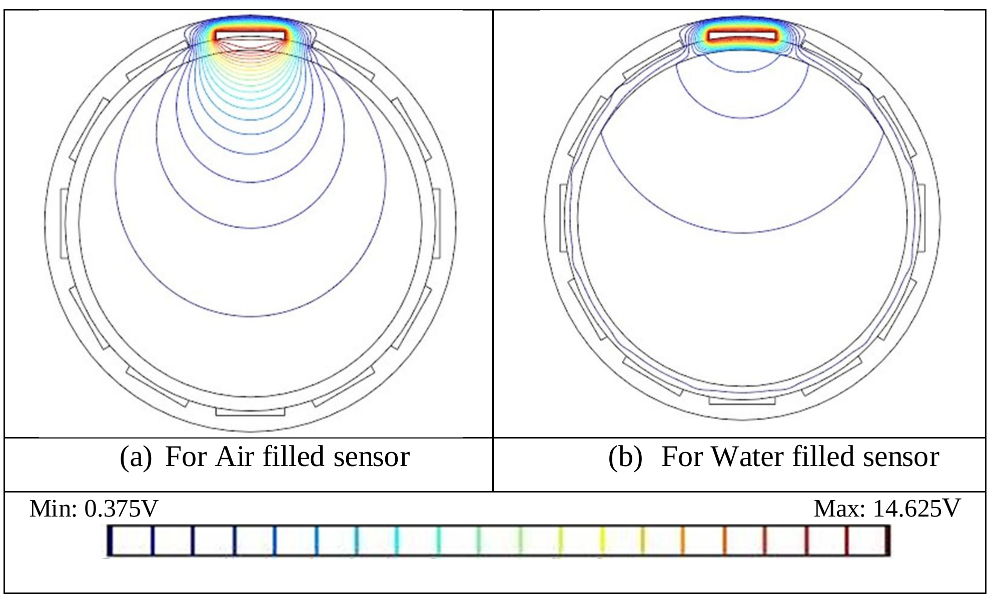

(a) For Air filled sensor | (b) For Water filled sensor

Figure 5.13: Equipotential Contour Plot for (a) Air and (b) Water in *2D*.

5.4.2 Effect of Radial Guards

The main effect of the grounded shield is to confine the field lines within the pipe so that they cannot travel from the source to detecting electrodes through the pipe wall as shown in Figure 5.14 (a) and (b). It can be observed that the field lines that travel through the pipe wall, crossing the equipotential lines perpendicularly die at the grounded radial tracks before they reach the detecting electrodes. The external field lines are neutralised by the grounded screen. So the capacitance measured between these electrodes is only due to the field lines that cross the internal sensing domain of the pipe. This drop in field lines causes a decline in the charge of the detecting electrodes that may results in lower capacitance.

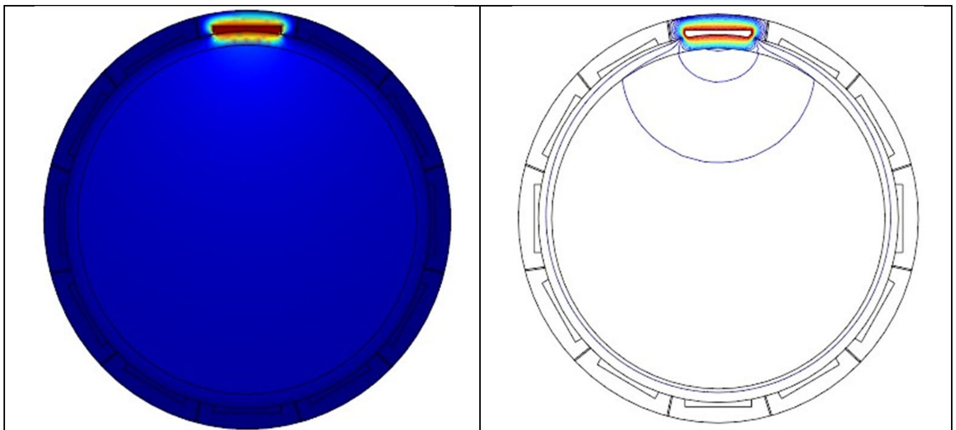

(a) Electrical Field	(b) Equipotential lines

Figure 5.14: Water Filled Sensor with Radial Guards (a) Electrical Field and (b) Equipotential Lines Distribution for (*2D*).

Figure 5.15 shows the graph plotted for the standing capacitances between the shielded and non-shielded sensor for air filled pipe. Figure 5.16 shows the adjacent electrode capacitances as a function of the permittivity of the material within the sensing zone/domain for shielded and non-shielded ECT sensors. The capacitances of the ECT sensor without guards are more sensitive to the material used within the sensing zone. The use of guards significantly reduces the capacitance, which is beneficial.

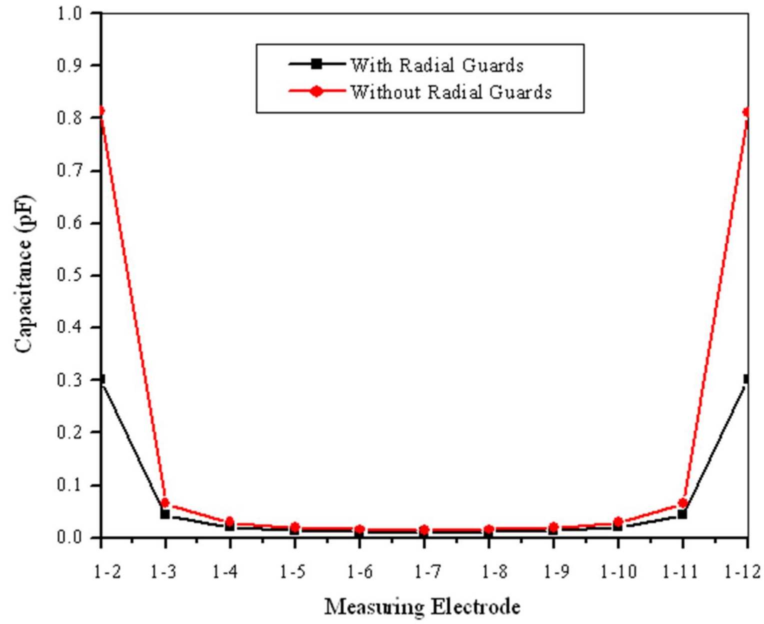

Figure 5.15: Standing Capacitance for a Sensor Having Radial and Non-radial Guards.

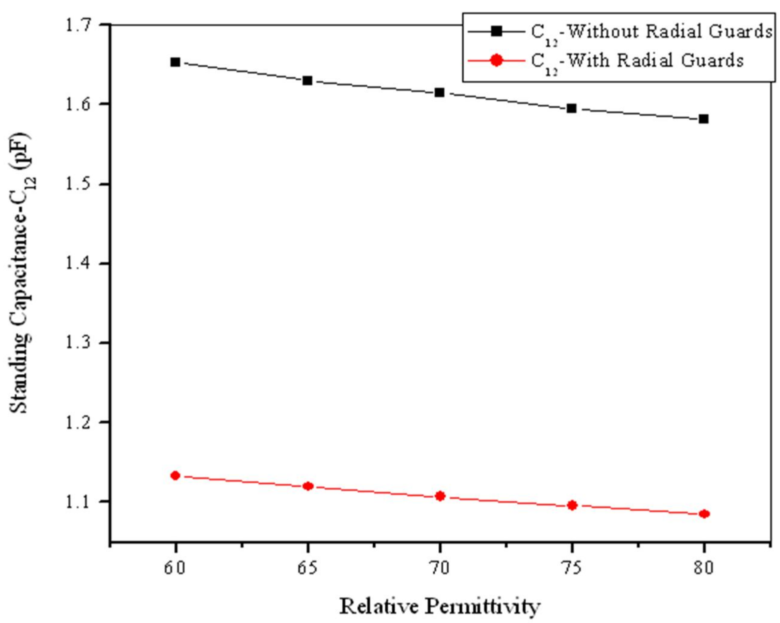

Figure 5.16: Sensor Performance with and without Guards for Adjacent Electrodes.

5.5 Application of Distribution Models

The measured capacitances are usually normalised before being used for any application. The capacitance measured depends on the permittivity of the materials between the electrodes. Their relation can be linear or non-linear in nature. The conventional normalization approach assumes that the distribution of the two materials is in parallel and the normalised capacitance is the linear function of the measured capacitance [89]. An improved normalization approach is derived from a series sensor model by modeling the sensor capacitances as two capacitances in series. The normalization equation has been mentioned in section *3.2.4.2.* The various permittivity models used in this study for the estimation of void fraction are the series, parallel, Maxwell and combined model.

5.5.1 Series Model

The theoretical description of this model has been done in section *3.2.4.2.* When the graph is plotted for the normalised capacitance i.e. obtained by using equation (3-14) in Figure 5.17, it demonstrates that the normalised capacitance using this model lies in the permissible range of ‘0’ to ‘1’. The normalised capacitance for the Series model follows the range from $0.635 \geq C_n \geq 0.69$. The X-axis corresponds to the capacitance electrode pairs (for 12 electrodes M = 66) as listed in Table 4.4 while Y-axis indicates the normalised capacitance obtained Series (ζ) model. The graph is plotted for different flow rates of deionised water at constant air flow rate i.e. 1.5 LPM. It can be seen from the graph that almost all follow the similar trend except the case in which deionised water flow rate is 3.5 LPM, shows the maximum values of normalised capacitance and also the behaviour of the curve is different from others.

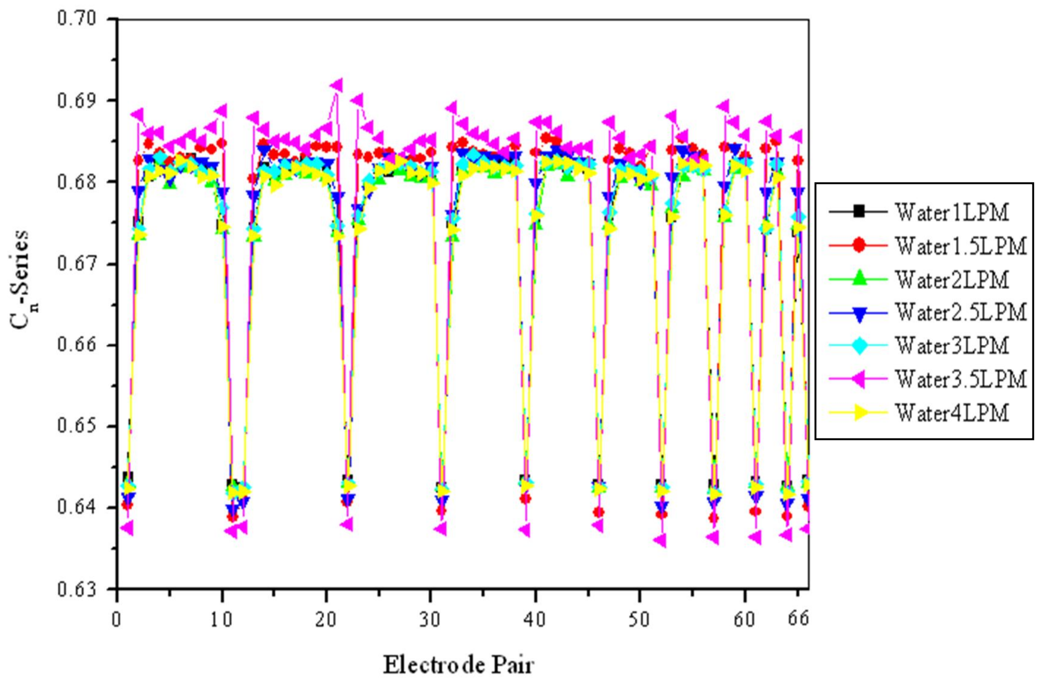

Figure 5.17: Normalised Capacitance Obtained *via* Series model (ζ) at Q_g = 1.5 LPM.

5.5.2 Parallel Model

The theoretical description of this model has been done in section *3.2.4.2*. Parallel model was considered as a conventional normalisation approach in which the distribution of the two materials is in parallel. On the application of equation (3-16), the graph is plotted between the normalised capacitance (i.e. Y-axis) and the 66 capacitance electrode pairs (i.e. X-axis) in Figure 5.18. It illustrates that the normalised capacitance following the acceptable range from 0.655 ≥ C_n ≥ 0.685. It can also be perceive from the graph that almost all the cases follow the similar trend, while the case in which air flow rate is 3 LPM shows the maximum value for 1-adjacent electrode pair.

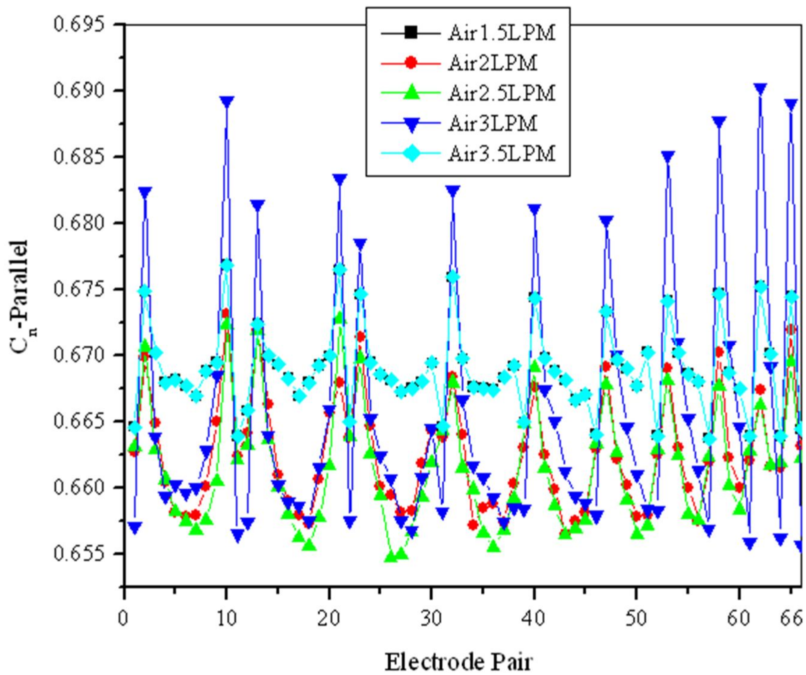

Figure 5.18: Normalised Capacitance Obtained *via* Parallel model (λ) at Q_w=1.5 LPM.

5.5.3 Maxwell Model

Maxwell model is a combination of previous two models. A detailed theoretical description for this model has been explained in section *3.2.4.2*. The graph plotted between the normalised capacitance (i.e. obtained by using equation (3-18)) and the capacitance electrode pair is shown in Figure 5.19. It implies that the normalised capacitance particularly for Maxwell follows the range 0.650 ≥ C_n ≥ 0.685 that lies in between '0' to '1'. The graph represents that the case in which water flow rate is 1, 1.5 and 2.5 LPM following similar trend, while the test case in which deionised water is at 2, 3, 3.5 and 4 LPM follows different trend.

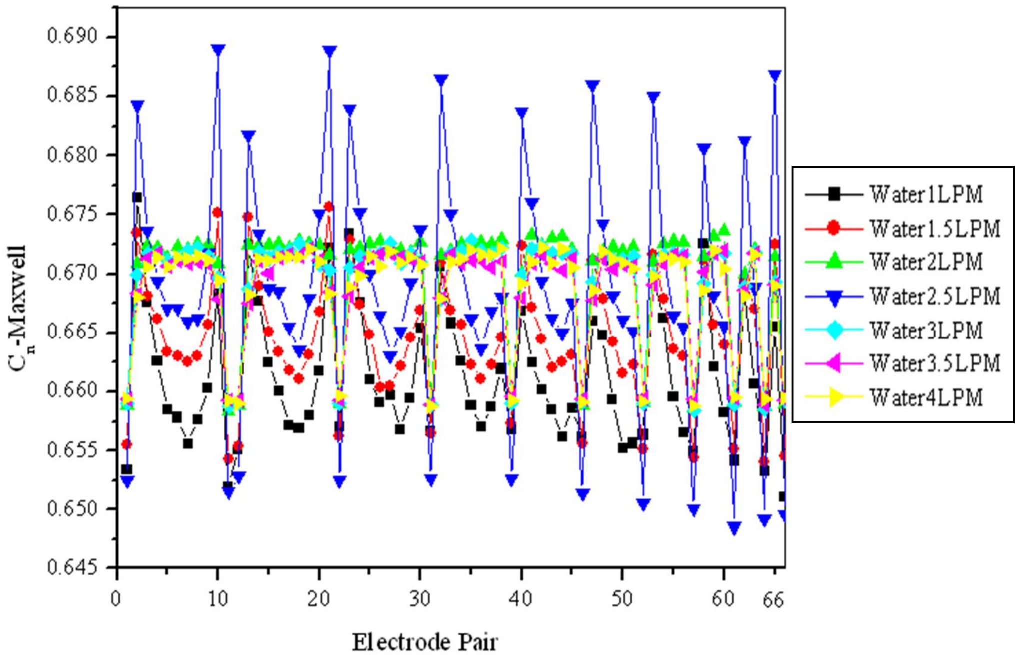

Figure 5.19: Normalised Capacitance Obtained *via* Maxwell model (Φ) at Q_g = 2.5 LPM.

5.5.4 Combined Model

The analysis for this model has been done in two ways; one by plotting the graph between all the possible number of measurements and normalised capacitances by varying the values of α for the test case in which air is 1.5 LPM and deionised water is 2 LPM, as shown in Figure 5.20. The normalised capacitance behaviour for this particular model can be seen from the Figure 5.20 that as soon as the concentration is increasing, C_n for all the electrode pairs are decreasing except for the adjacent electrode which is increasing on the increase in concentration.

Figure 5.21 represents the combined model result by varying the values of α (is representing the concentration of water) at 0.1, 0.3, 0.5 and 0.7 for adjacent electrode pairs for the test case when air is varying from 1.5 to 3.5 LPM and deionised water is constant at 2 LPM.

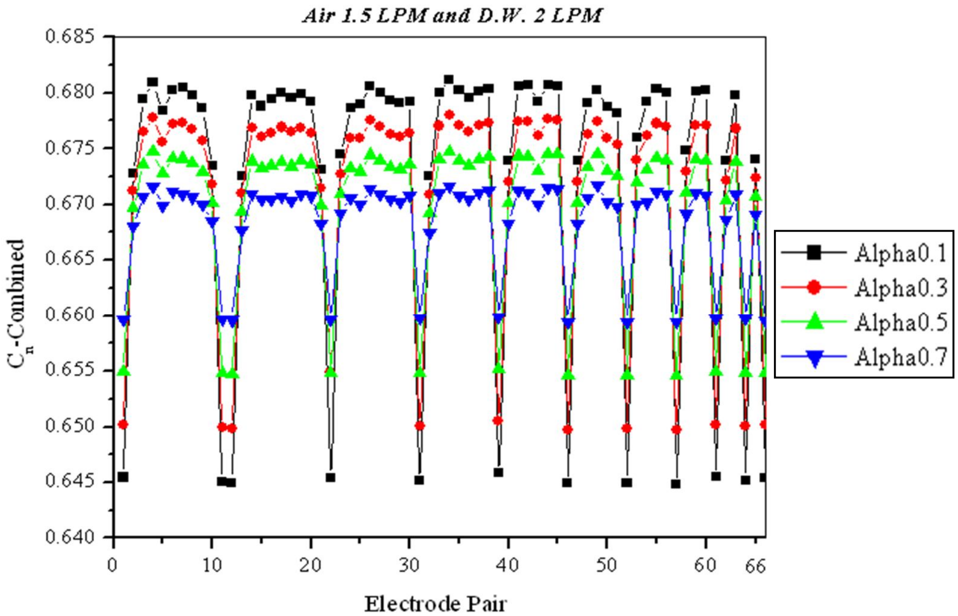

Figure 5.20: Normalised Capacitance Obtained from Combined Model (δ) for α = 0.1, 0.3, 0.5 and 0.7.

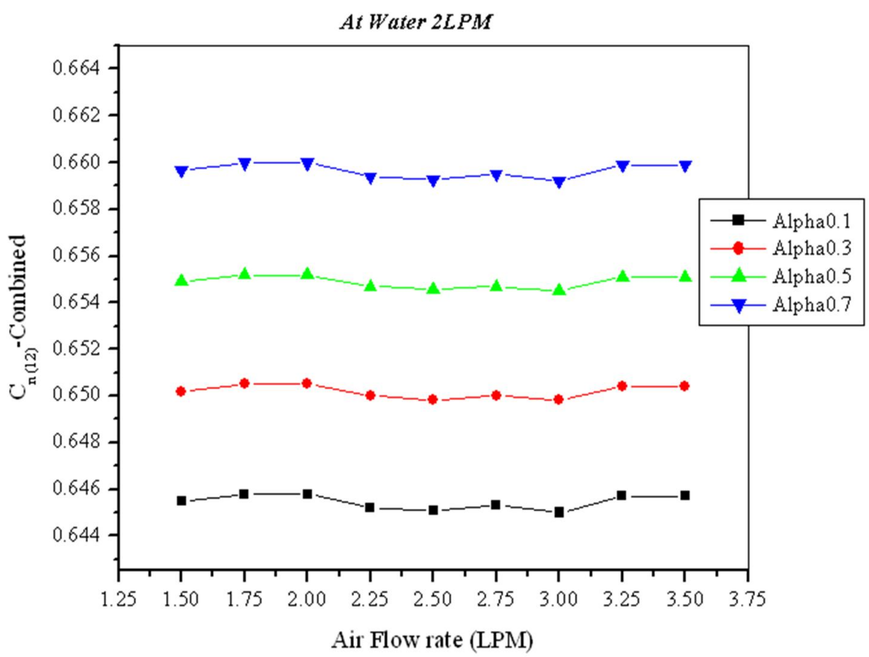

Figure 5.21: Comparison of Normalised Capacitances for Adjacent (C_{12}) Electrodes at Different Values of α.

5.5.5 Normalised Capacitance for Different Electrode Combinations

The preceding section covers all the distribution models individually, while in this section there will be an analysis based on the comparison between the distribution models at different conditions which were defined previously. Initially Figure 5.22 shows the comparison between the parallel, series, Maxwell and combined models for different electrode combinations. The graph is plotted between the air flow rate in LPM keeping the water flow constant at 2 LPM and the normalised capacitances for adjacent (C_{12}), 1-adjacent (C_{13}) and opposite (C_{17}) electrode pairs are shown.

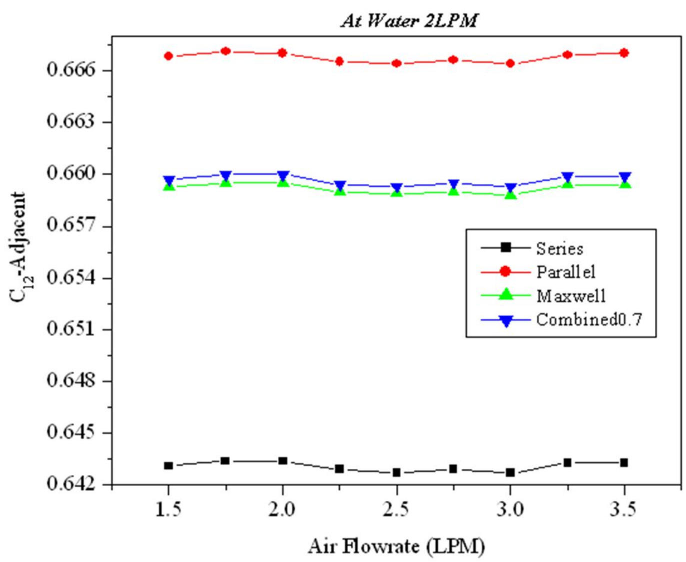

(a) C_{12}-Adjacent Electrode Pair

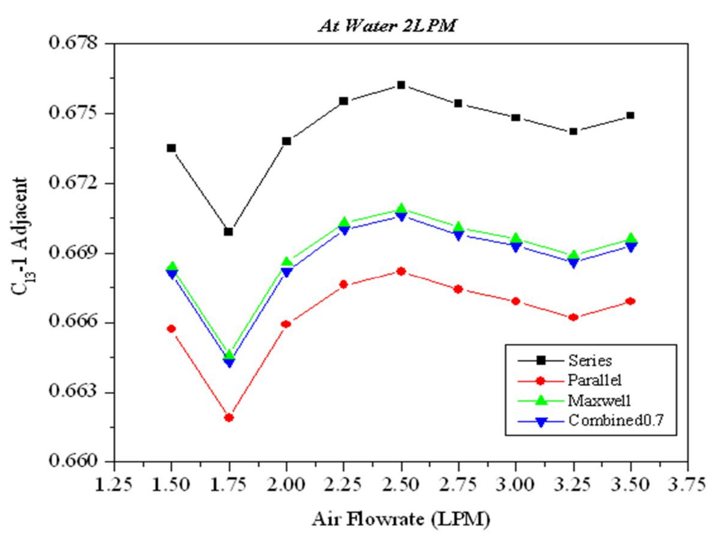

(b) C_{13}- 1 Adjacent Electrode Pair

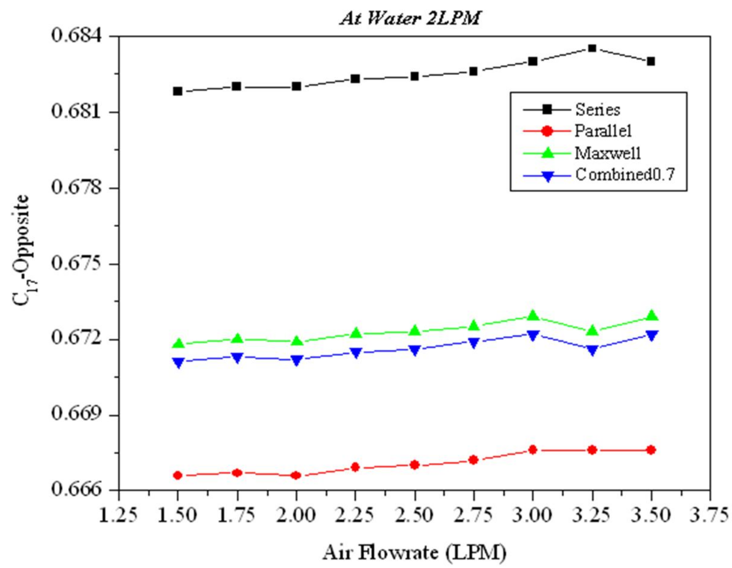

(c) C_{17}-Opposite Electrode Pair

Figure 5.22: Normalised Capacitance *versus* Air Flow Rates for (a) Adjacent (b) 1-Adjacent and (c) Opposite Electrodes at Q_w = 2LPM.

It has been observed from the Figure 5.22 that the parallel model follows the lowest range for normalised capacitances for 1-adjacent and opposite electrode pairs; while for adjacent combination it shows the highest value of C_n. For series model the condition will be opposite to the parallel model; while Maxwell and combined models lie in between them for each combination pairs. The trend followed by distribution models for adjacent electrode pairs in Figure 5.22 (a) initially increasing and then slightly decreasing pertaining to be in the range of $0.64 \geq Cn_{12} \geq 0.66$. However, in Figure 5.22 (b) the trend is almost increasing except for the few readings keeping them in the range of $0.664 \geq Cn_{13} \geq 0.676$. Finally, for the third combination i.e. shown in Figure 5.22 (c) signifies the best possible result obtained from the application of distribution models for the estimation of normalised capacitances. The range of C_{17} is from $0.666 \geq Cn_{17} \geq 0.682$.

5.5.6 Estimation of Measured Capacitance

The analysis based on the gas volume fraction (defined in section *2.9.1.2*) is described in this section. Based on the knowledge of GVF, the measured capacitance can be calculated for all the distribution models by the formula shown in section *3.2.4.2*. Figure 5.23, 5.24 and 5.25 shows the measured capacitance for the parallel, series, Maxwell and combined models for adjacent, 1-adjacnet and the opposite electrode pairs respectively.

Figure 5.23 shows that on increasing the gas volume fraction from 35% to 70%, the measured capacitance for adjacent (C_{12}) electrodes for all the distribution models has been decreased. The key observation of this plot is that the Maxwell model possesses the highest value for measured capacitance as compared to all the remaining models. The range for the adjacent measured capacitance lies from $1.60 \geq Cm_{12} \geq 1.71$.

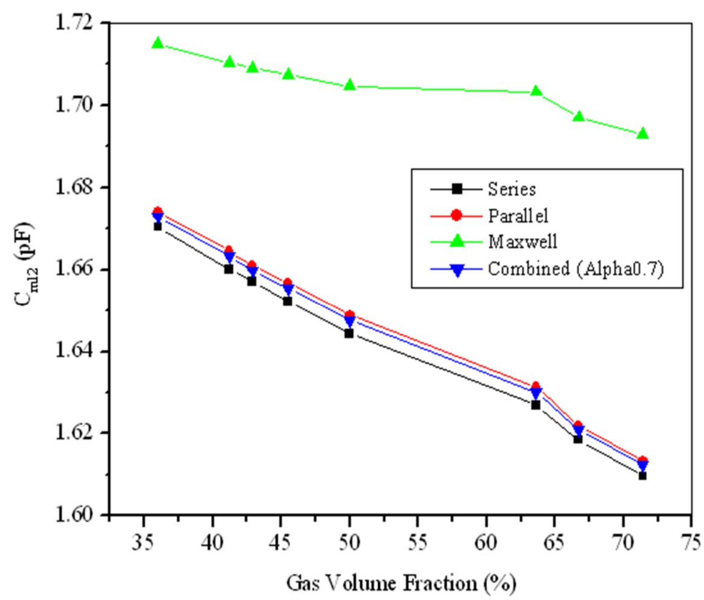

Figure 5.23: Measured Capacitance for Adjacent Electrode (C_{m12}).

Figure 5.24 shows the graph plotted between the GVF and the measured capacitance for all the distribution models in which electrode combinations are adjacent (C_{13}) apart from each other. On increasing the GVF, the measured capacitance also increases following the range from $0.9 \geq Cm_{13} \geq 0.913$.

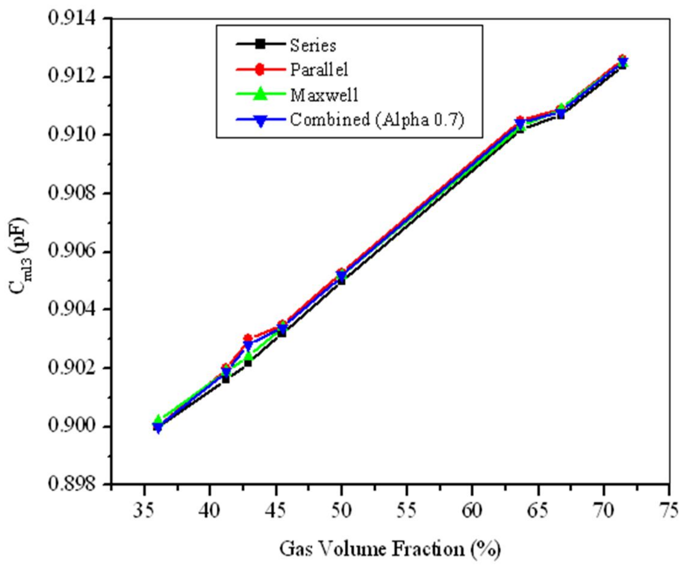

Figure 5.24: Measured Capacitance for 1- Adjacent Electrode (C_{m13}).

Figure 5.25 is another representation of the GVF and measured capacitance using the distribution models for the opposite (C_{17}) electrode combinations. The opposite electrodes in ECT shows the smallest capacitance values as can be observed in the plot. The relationship between GVF and measured capacitance is proportional i.e. by increasing the GVF; the measured capacitance also increases proportionally in the range of $0.815 \geq Cm_{17} \geq 0.835$.

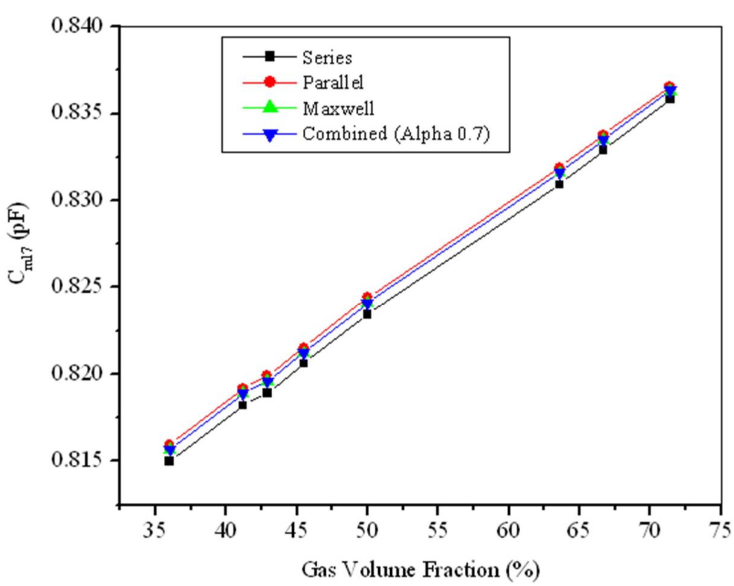

Figure 5.25: Measured Capacitance for Opposite Electrode (C_{m17}).

5.6 Void Fraction Calculation Using Normalised Capacitance

The average voidage can be calculated by summing all the normalised capacitance values for one image frame dividing by the sum of the normalised capacitances when the sensor filled with higher permittivity material. By using equation (3-26), the volume ratio is calculated for different flow rates of air when deionised water was fixed at 1.5 LPM. These measurements vary with different distribution models calculation based on different flow rates of air and deionised water. Figure 5.26 shows the graph plotted between the air flow rates in LPM and the voidage calculation in %. The application of all the models for the voidage calculation reveals that they all predict the same trend of plot. On increasing the air flow rate, initially the voidage kept on increasing then suddenly it decreases at 3 LPM of air and then increases again at 3.5 LPM of air. It was also observed that the Parallel model shows the maximum range of voidage values while the Series model shows the minimum range. Combined model for $\alpha=0.7$ has found to be very close to the Maxwell model which is in between the series and parallel models. The range of voidage values based on the normalised inter-electrode capacitance measurements is from 0.989 to 0.99 i.e. less than a permissible range of 0 to 1.

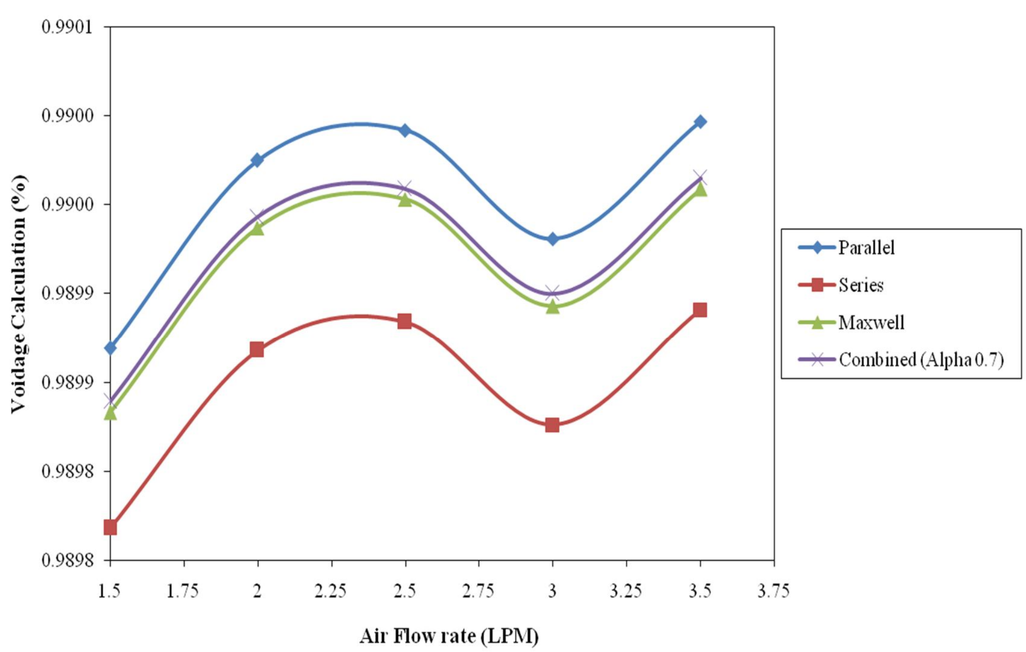

Figure 5.26: Voidage Calculation for the Distribution Models at Q_w=1.5 LPM.

5.7 Void Fraction Calculation Using Normalised Pixels

The void fraction can also be calculated by using the normalised pixel values in the reconstructed ECT image. In the case of calculation from image pixels, this is done be summing the values of the individual pixels in the ECT image for the required image frame and dividing this figure by the number of pixels. The more detail on the estimation of void fraction using pixels is given in section *2.4.3* and *3.2.4.4.*

Figure 5.27 (a)-(g) shows the result for void fraction obtained from image pixels based on different flow rates of air and deionised water. The range it covers lies in between $0.001 \geq \alpha \geq 0.012$.

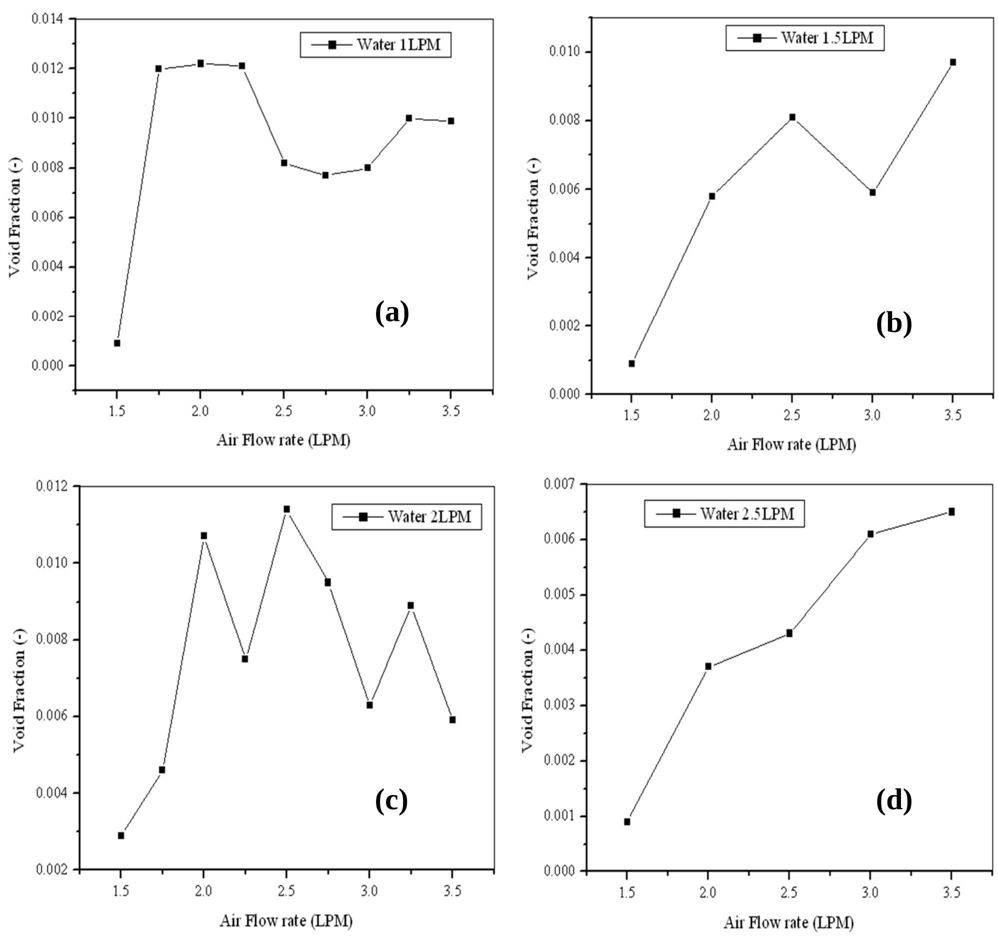

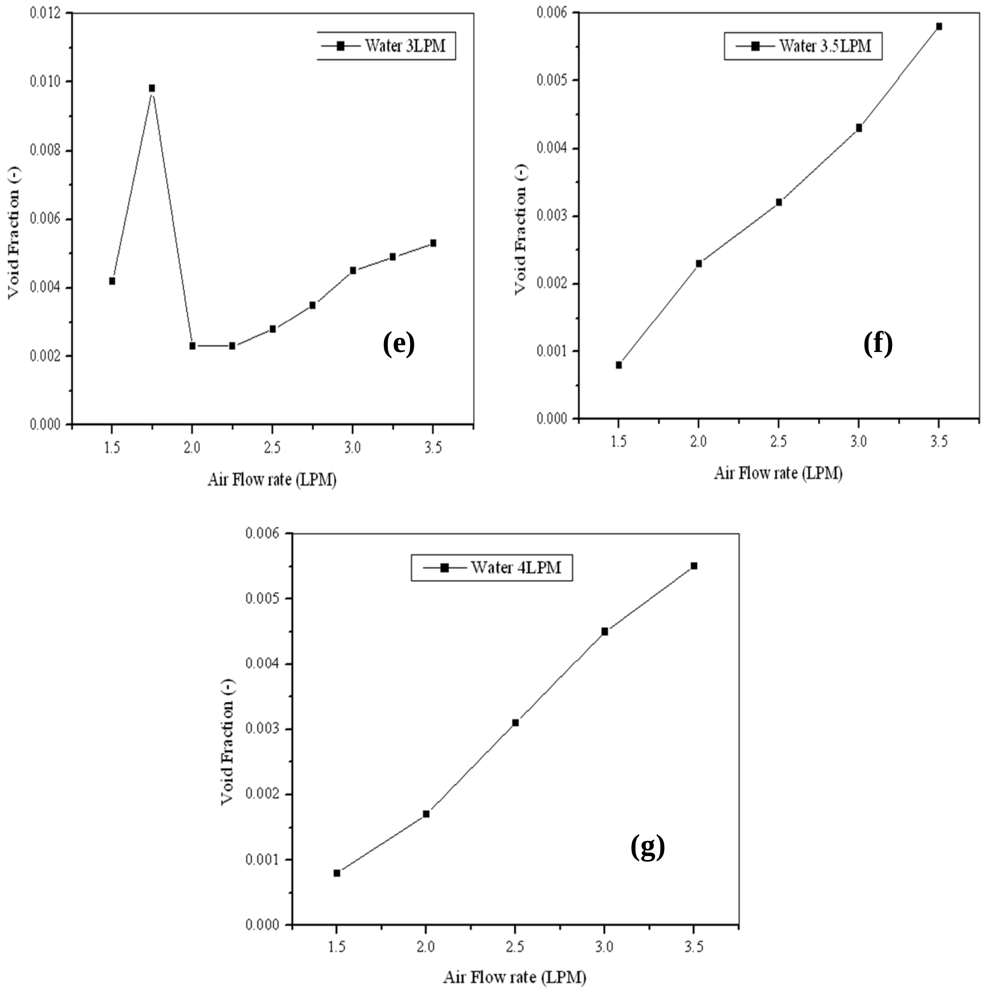

Figure 5.27: Void Fraction Calculation Using Image Pixels at (a) Q_w =1 LPM, (b) Q_w =1.5 LPM, (c) Q_w =2 LPM, (d) Q_w =2.5 LPM, (e) Q_w =3 LPM, (f) Q_w=3.5 LPM and (g) Q_w =4 LPM.

5.8 Void Fraction Characterization

This part of the thesis deals with the estimation and comparison of the void fraction values obtained from the experimental measurements along with the empirical results for the vertical upward air-water two-phase flow conditions.

5.8.1 Estimation of Void Fraction Using Delta-P

The following section covers the results obtained for the void fraction calculation from the differential pressure transducer. The superficial gas velocity has found to be a critical parameter which affects the void fraction significantly. In order to test out this phenomenon, the superficial gas velocity was varied in the range of 1.31 cm/sec to 3.05 cm/sec. The results shown in Figure 5.28 are from experiments that were run over a series of air and deionised water flow rates and Table 5.5 contains the measured values. The graphical analysis shows that as the superficial gas velocity (U_{sg}) increases, the discrete-dispersed bubble flow regime starts to develop, and the void fraction reaches its maximum value, keeping the superficial liquid velocity (U_{sl}) as constant. The multiple orifice nozzle ensures a uniform gas distribution, so the regime is homogenous at superficial gas velocities lower than 3 cm/sec. This is indicated by the linearity of λ_g versus U_{sg}.

Table 5.5: Void Fraction Measurement Using ΔP

U_{sl} / U_{sg} (m/sec)		0.0131	0.0174	0.0218	0.0262	0.0305
0.0131	**ΔP (Pa)**	3150.904	3095.75	2992.325	2978.54	2930.272
	λ (-)	0.055315	0.07185	0.102859	0.106992	0.121463
0.0218	**ΔP (Pa)**	3171.6	3099.9	3019.9	2992.325	2957.16
	λ (-)	0.04911	0.070606	0.094591	0.102859	0.113402
0.0305	**ΔP (Pa)**	3199.2	3123.33	3047.5	3001.3	2975.1
	λ (-)	0.040835	0.063582	0.086316	0.100168	0.108023

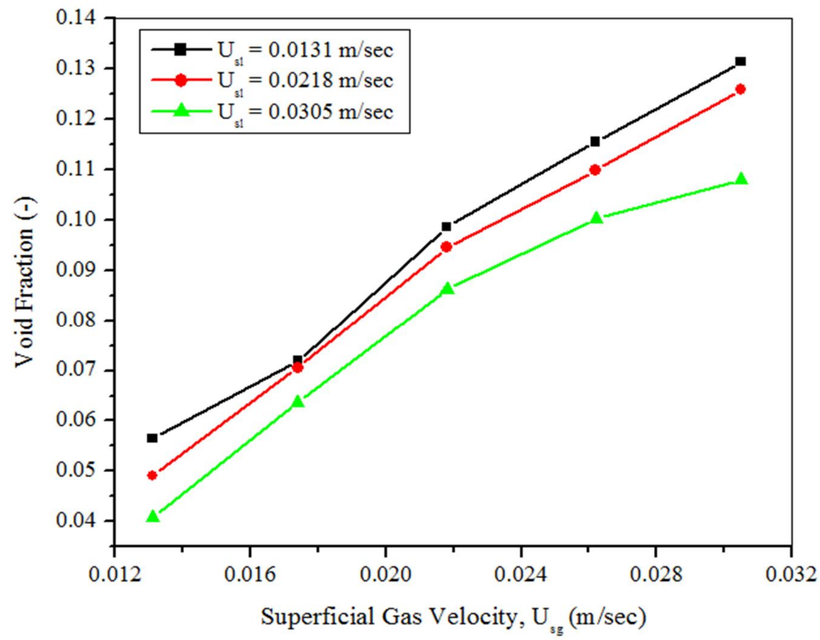

Figure 5.28: Void Fraction for an Air-Water System Using ΔP.

On applying the *2nd* order polynomial regression analysis the relationship between the void fraction and superficial gas velocity can be defined by the following expression (5-3):

$$Y=A_0 + A_1x + A_2x^2 \tag{5-3}$$

where, $Y= \lambda$, $x=U_{sg}$ and A_0, A_1 and A_2 are the coefficients of the polynomial whose values are given in Table 5.6.

Table 5.6: Values for Equation (5-3) at Different U_{sl}

U_{sl} (m/sec)	A_2	A_1	A_0	R^2
0.0131	-118.2	8.994	-0.043	0.970
0.0218	-142.8	9.917	-0.056	0.993
0.0305	-146.5	10.31	-0.069	0.998

Figure 5.29 shows the effect of superficial gas velocity on the void fraction and the observations are in good agreement with the results of other investigations (Akita and Yoshida, 1973; Jin *et al*., 2007), thus verifying the validity and effectiveness of the measurement technique. The void fraction is initially a linear function of the superficial gas velocity, typical of the homogenous bubble flow regime. It can be observed from other researchers' [15], [88] findings that with increase in superficial gas velocity a point is reached where the transition to other flow regime occurs (i.e. a heterogeneous regime).

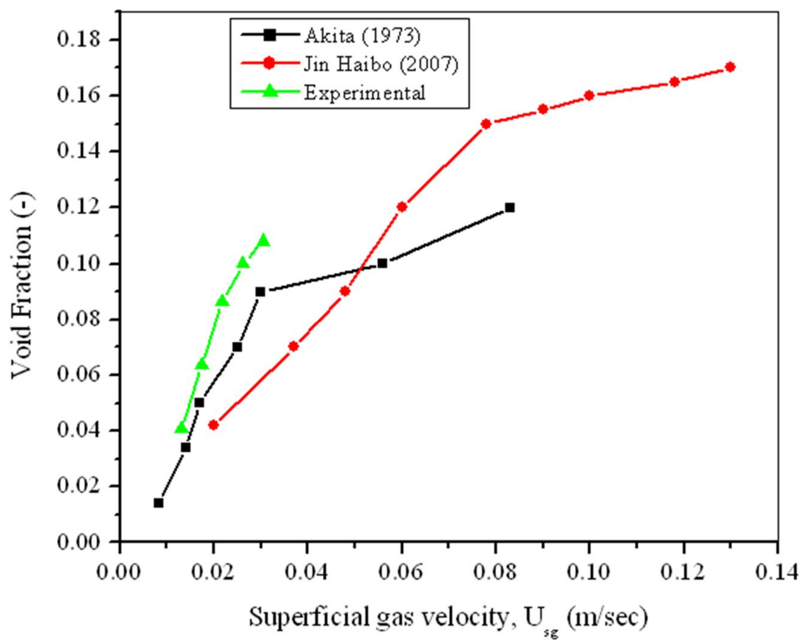

Figure 5.29: Comparison of Void Fraction Values as a Function of U_{sg} with Other Studies.

The relationship between the differential pressure and the void fraction is shown in Figure 5.30. The full line in the figure was determined from applying a linear regression to the data and the correlation coefficient squared (R^2) found was 0.99. The linear fit error is in the range of ±0.1 to ±0.6. The expression obtained from the linear regression analysis is shown in equation (5-4):

$$y = 3329.14 - 3326.6x \tag{5-4}$$

where, $y = \Delta P$ and $x = \lambda$.

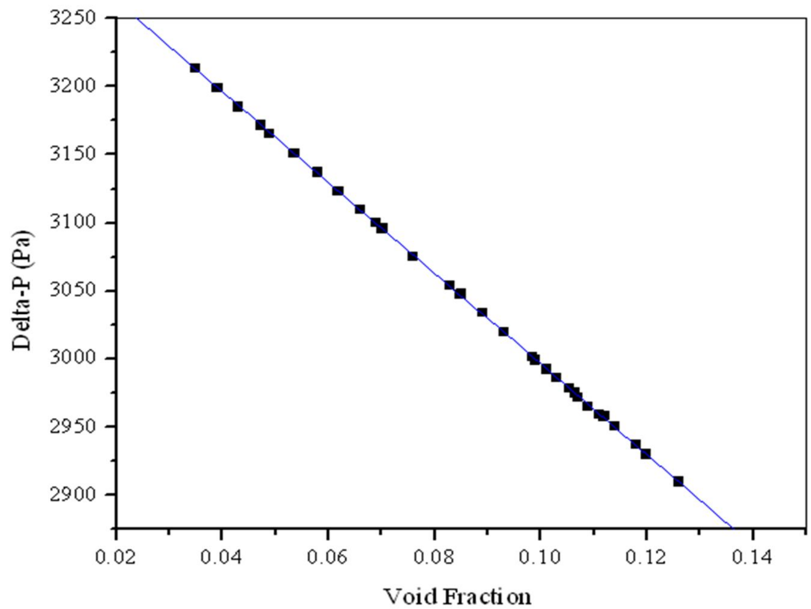

Figure 5.30: Void Fraction *versus* ΔP.

5.8.2 Estimation of Volume Void Fraction Using Photograph

Based on the knowledge of volumetric void fraction, this current study also calculated the void fraction by using the photographic technique as discussed in section *2.4.4*. Figure 5.31 shows the plot between air flow rate and void fraction obtained from the photographic technique that is calculated by using the below mentioned formula in equation (5-5) [2]:

$$\lambda_g = \frac{V_g}{V_T} \tag{5-5}$$

where; $V_g = \frac{4}{3}\pi r^3 \times n_b$ is the volume of gas phase

$V_T = \pi r^2 \times l$ is the total volume of the cylinder

r is the radius of the bubbles

n_b is the average number of bubbles present in cylinder and

l is the length of electrodes.

The experimental results of void fraction in upward vertical air-water bubble flow were measured from the test section for void fraction measurement and flow visualisation. The variations of the void fraction with air and deionised water flow rates for upward vertical flow were established from the above mentioned equation as shown in Figure 5.31. It can be observed that low air flow rate caused rapid increase in void fraction while void fraction increase gradually with increasing air flow rate. The void fraction for the bubble flow regime for the current experimental setup ranges from $0.02 \leq \lambda_g \leq 0.12$.

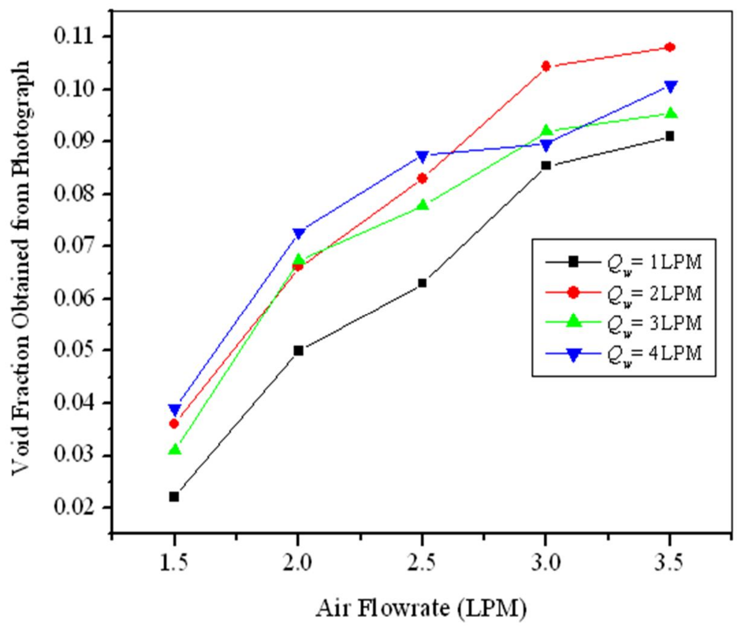

Figure 5.31: Void Fraction for an Air-Water System Using Photographic Technique.

5.8.3 Application of Drift-Flux Model

The drift-flux model is a widely used model due to its simplicity and applicability in two-phase flows [30]. The model is found to predict the two-phase flow characteristics like void fraction. The drift-flux model has long been used to model vertical two-phase systems. Due to the considerable importance of drift-flux model in predicting the two-phase flow characteristics, this study also used this model to predict the void fraction.

Due to the importance of void fraction in influencing the characteristics of two-phase flow in pipes, different researchers proposed different correlations to predict the void fraction. Figure 5.32 to 5.34 show the trend between the U_{sg} and void fraction obtained from ΔP keeping the liquid velocity at constant. It was visually (and intuitively) observed that the void fraction increased proportionally and fairly smoothly as the flow rate increased. The experimental results obtained from ΔP has compared with the drift flux model defined by Zuber *et al*. (1967) and Hibiki *et al*. (2003). When the drift-flux model was applied, it was found that the experimental results obtained from delta-P for this study were in good agreement with the results obtained by this model for different values of C_0 and V_{gj} as mentioned by some previous researchers [32], [34]. The details of the drift flux model and the values for C_0 and V_{gj} has already been discussed in section *2.4.2*. The below mentioned figures indicates that the void fraction correlation follows the increasing trend which is in accord with the experimental results.

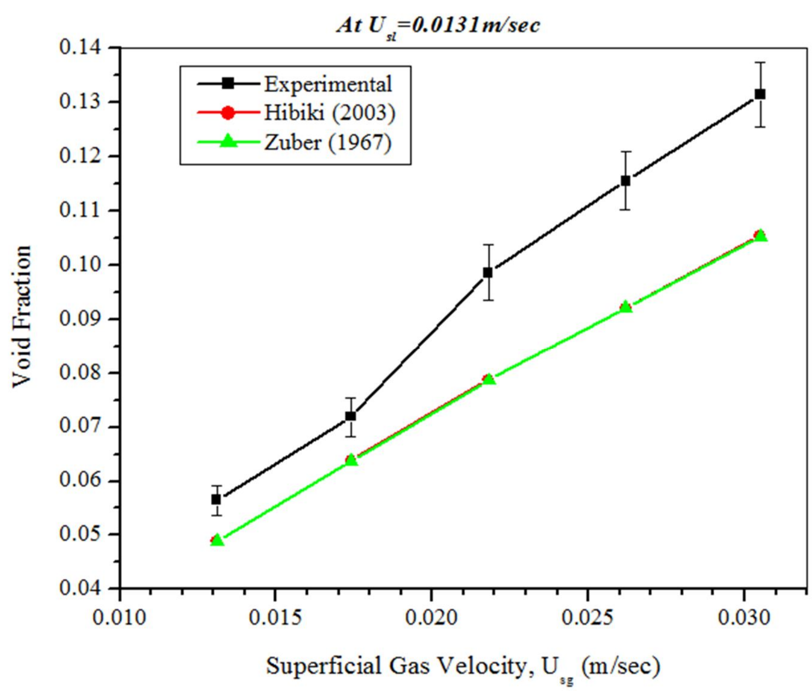

Figure 5.32: Void Fraction Values as a Function of U_{sg} at U_{sl} = 0.0131 m/sec. Error for Experimental Values is in The Range of ±0.3 to ±0.6%.

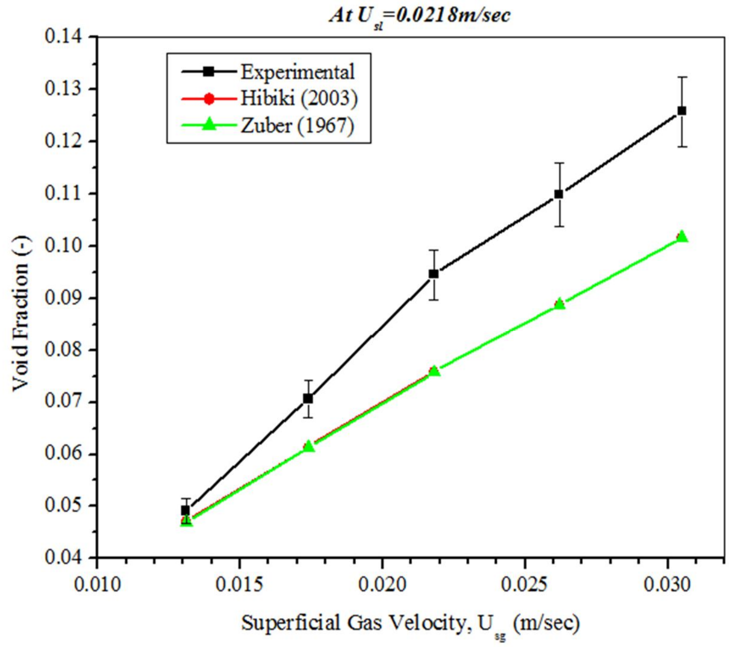

Figure 5.33: Void Fraction Values as a Function of U_{sg} at $U_{sl} = 0.0218$ m/sec. Error for Experimental Values is in The Range of ±0.2 to ±0.5%.

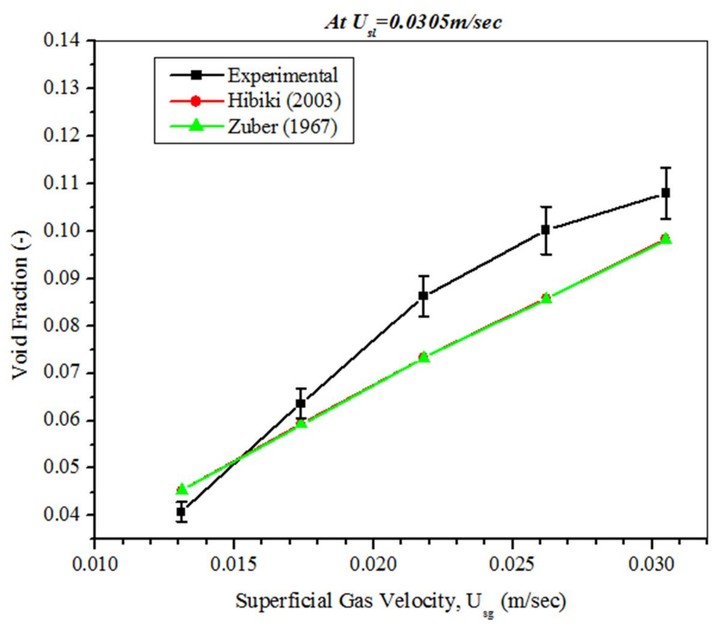

Figure 5.34: Void Fraction Values as a Function of U_{sg} at $U_{sl} = 0.0305$ m/sec. Error for Experimental Values is in The Range of ±0.2 to ±0.5%.

5.8.4 Comparison between Measured and Calculated Void Fraction

Figure 5.35 shows a plot between the measured values (obtained from delta-P) and calculated values (obtained from Drift-Flux model defined by [30]) of void fraction. The relation between the two relatively shows a good agreement. On applying polynomial regression the correlation coefficient R^2 was 0.972 and the maximum average percentage error lies within 20% which is tolerable. The results shown in the Figure 5.35 are from the experiments that were run over a series of air and deionised water flow rates. Their relationship can be defined by a 2^{nd} order polynomial expression.

$$Y = A_0 + A_1 x + A_2 x^2 \tag{5-6}$$

where, A_0, A_1 and A_2 are the coefficients of the polynomial whose values are given as:

- $A_0 = 0.03672$
- $A_1 = 0.03143$
- $A_2 = 4.77861$

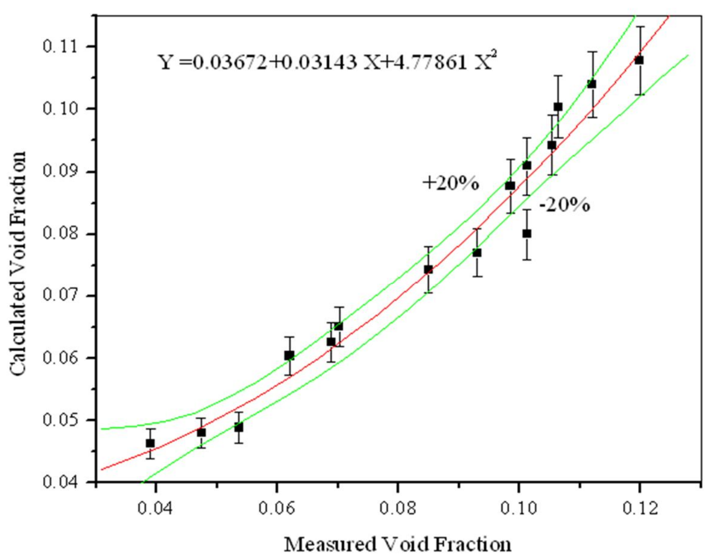

Figure 5.35: Comparison of Measured *vs.* Calculated Void Fraction Values in a 49.3mm Inner Diameter Vertical Column at Different Gas Flow Rates.

5.8.5 Effect of Liquid Properties on Void Fraction

The effect of using purified deionized water against regular tap water was studied in the 0.0493 m diameter column. The deionized water was obtained from a *Purelab Option Water Purification System* which produces general laboratory grade water with a resistivity of 18 Mega ohm-cm. The complete apparatus were washed with the same water before the actual runs. Figure 5.36 shows the difference in void fraction obtained by using with tap water and deionized water at different superficial gas velocities. The magnitude of the void fraction with the deionized water is lower than that obtained with regular tap water. The bubble sizes also observed in the column with deionized water were much larger and therefore, the holdup is lower. These observations are in consistent with the results mentioned in [18] who assert that the tap water produces coalescence of the bubbles. The percentage difference calculated between the two different types of water (i.e. deionised and tap water) was found to be in the range of 0.8 to 9.3%.

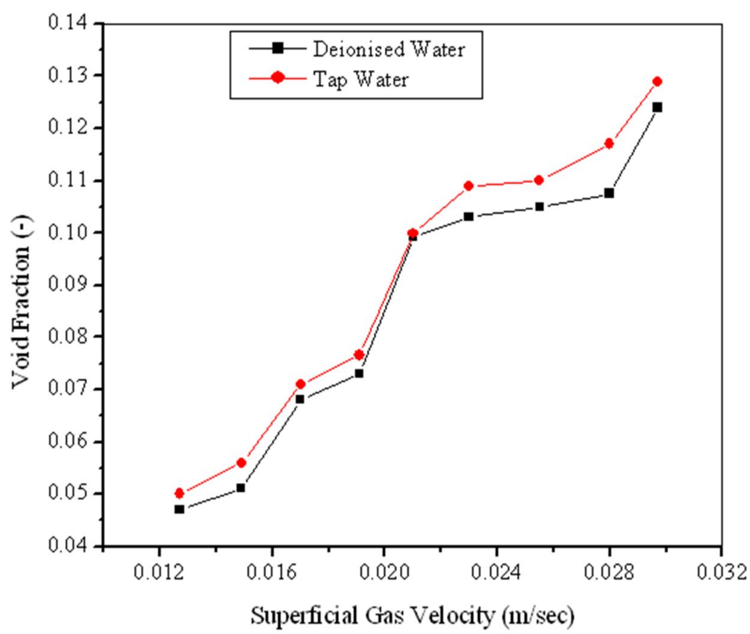

Figure 5.36: Effect of Liquid Properties – Tap Water and Deionized Water.

5.9 Comparison of ECT, ΔP and Photographic Void Fraction Measurements

This section covers the comparison between the void fraction measurements obtained from ECT, ΔP and Photographic methods. Table 5.7 shows the results based on different flow conditions of air and deionised water.

Table 5.7: Measurements of Void Fraction Using ECT, ΔP and Photographic Technique

Techniques	Water Flow Rate (LPM)	Air Flow rate (LPM)				
		1.5	2	2.5	3	3.5
ECT	1	0.0009	0.008	0.0082	0.0099	0.0122
ΔP	1	0.068	0.084	0.115	0.119	0.127
Photograph	1	0.0222	0.05	0.063	0.0854	0.091
ECT	1.5	0.0009	0.0058	0.0081	0.0090	0.0097
ΔP	1.5	0.0536	0.0702	0.10124	0.1054	0.1199
ECT	2	0.0029	0.0059	0.0063	0.0107	0.0114
ΔP	2	0.051	0.078	0.109	0.113	0.122
Photograph	2	0.036	0.0661	0.083	0.1043	0.10795
ECT	2.5	0.0009	0.0037	0.0043	0.0061	0.0065
ΔP	2.5	0.0474	0.0689	0.093	0.1012	0.112
ECT	3	0.0023	0.0028	0.0042	0.0045	0.0053
ΔP	3	0.045	0.068	0.09	0.105	0.113
Photograph	3	0.031	0.0674	0.0779	0.092	0.0954
ECT	3.5	0.0008	0.0023	0.0032	0.0043	0.0058
ΔP	3.5	0.039	0.062	0.085	0.0985	0.1064
ECT	4	0.0008	0.0017	0.0031	0.0045	0.0055
ΔP	4	0.037	0.059	0.086	0.101	0.111
Photograph	4	0.039	0.0728	0.0875	0.0896	0.1008

Based on the measurements mentioned in the Table 5.7, the graph has been plotted in Figure 5.37 (a)-(g) to compare their relationship and observe a trend of the measurements. It can be seen from the plots that they all follow the increasing trend and limiting the range of void fraction from $0 \geq \alpha \geq 0.14$ for the bubble flow regime in a 0.0493 m inner diameter and 0.41 m length bubble column.

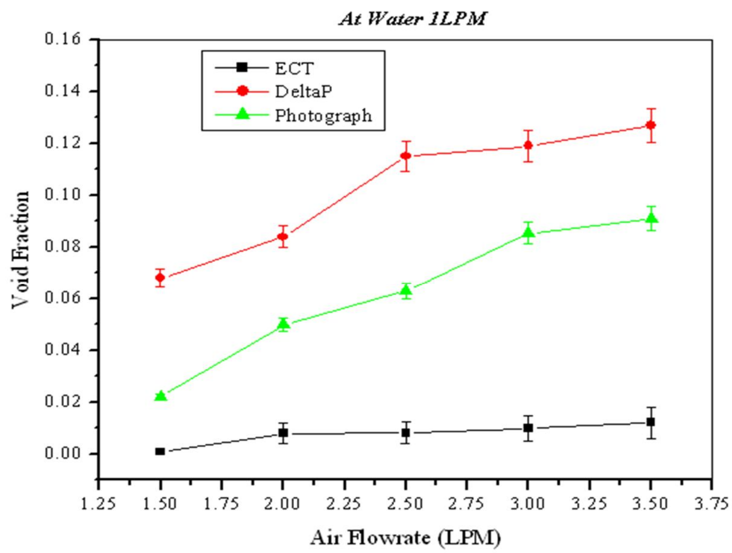

(a) Void Fraction Measurement at Q_w = 1LPM.

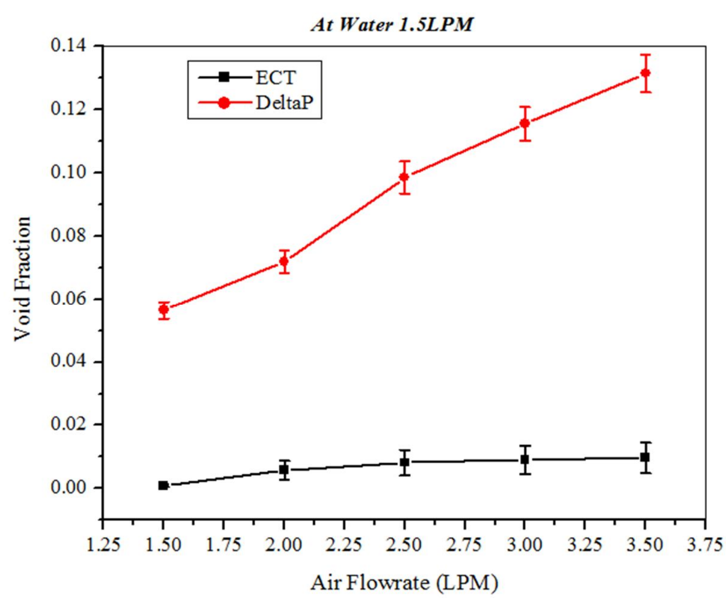

(b) Void Fraction Measurement at Q_w = 1.5LPM.

As it can be seen from the figure that the ECT follows the lowest range of void fraction because the flow rates for air and deionised water used in this experimental rig are in limited range. If the higher range of flow rates would be used than this measurement span for ECT void fraction could be improved.

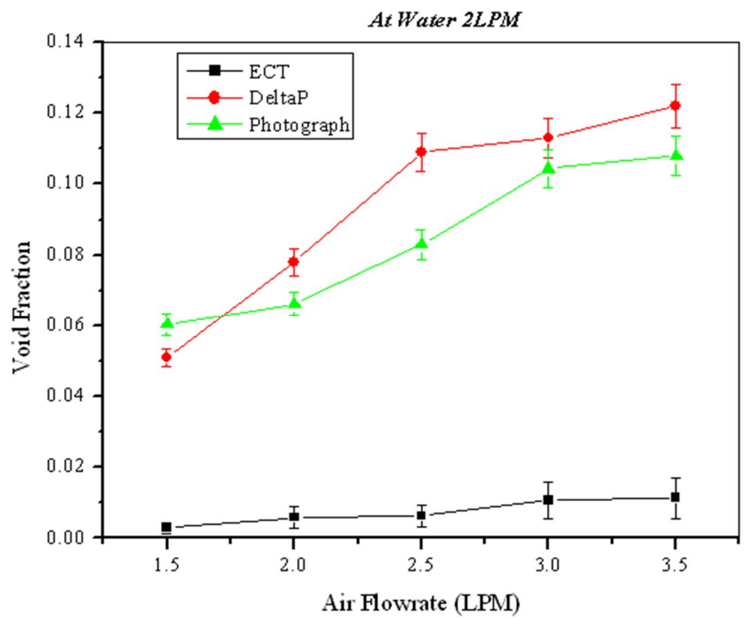

(c) Void Fraction Measurement at Q_w = 2LPM.

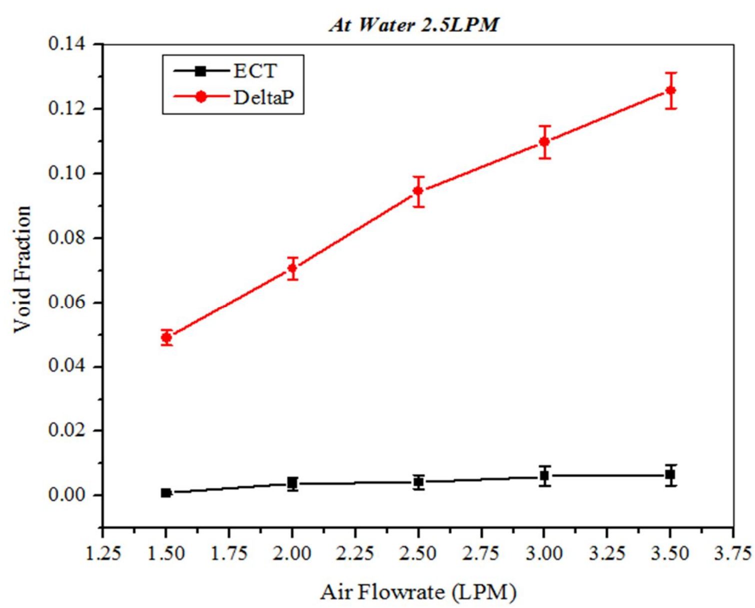

(d) Void Fraction Measurement at Q_w = 2.5LPM.

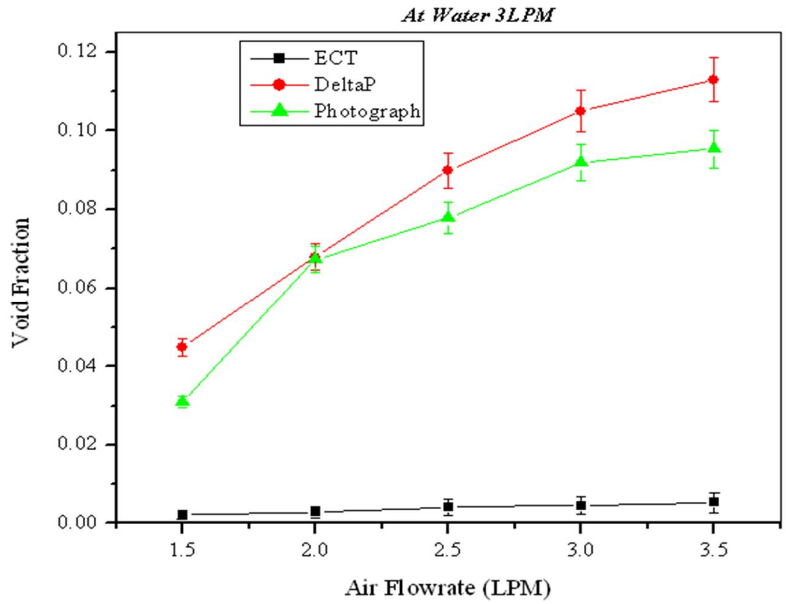

(e) Void Fraction Measurement at Q_w = 3LPM.

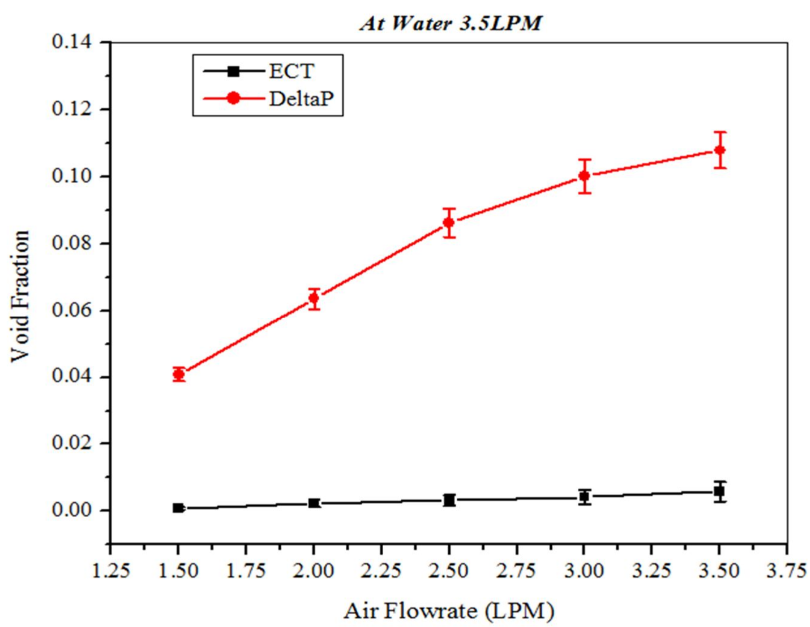

(f) Void Fraction Measurement at Q_w = 3.5LPM.

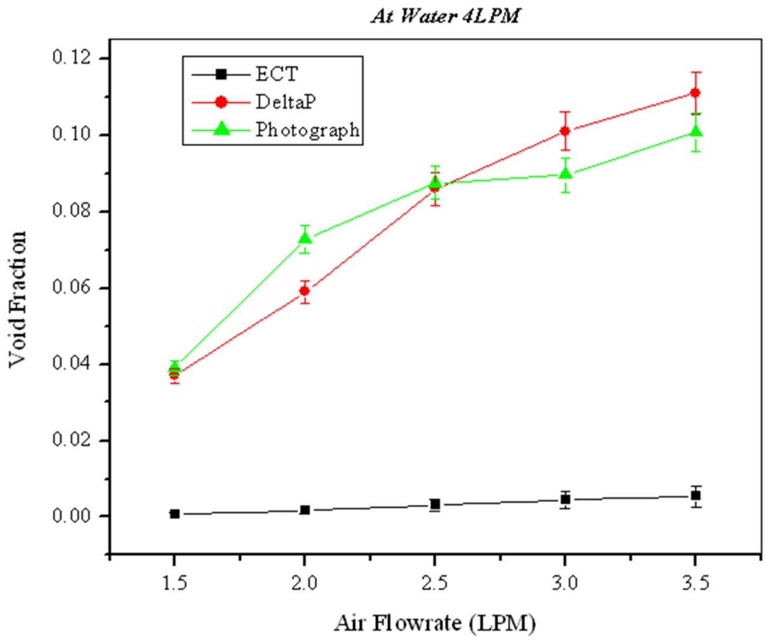

(g) Void Fraction Measurement at Q_w = 4LPM.

Figure 5.37: Void Fraction Comparison of ECT, ΔP and Photographic Techniques.

Figure 5.38 demonstrates the difference between the void fraction measurement obtained from ECT and ΔP cases as mentioned in Table 5.7 relative to the flow rates of air and deionised water. The plot shows the number of measurements versus the difference in measurement in terms of percentage on X-axis and Y-axis respectively. The absolute difference between the two methods is not greater than 12%.

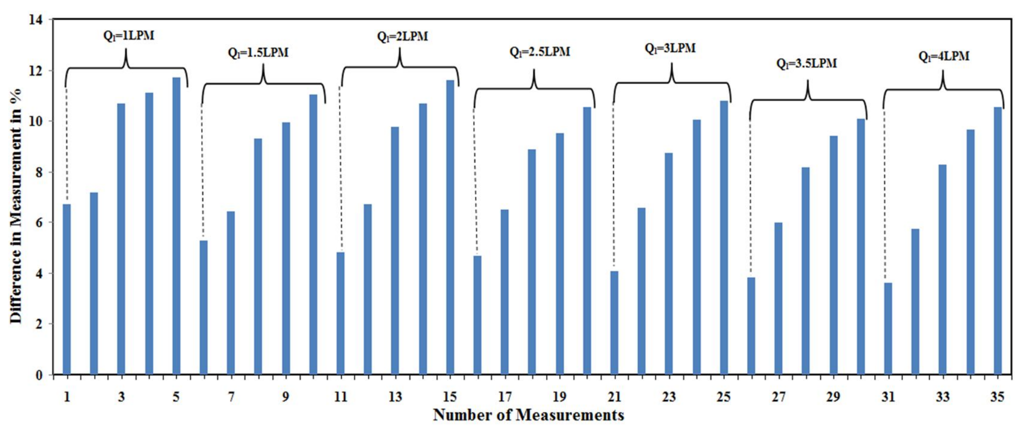

Figure 5.38: Absolute Difference in Void Fraction Obtained from ECT and ΔP.

5.10 Comparison between Experimental and Simulated Data

To verify that the 2D model is representative for the real physical sensor, measurements are performed. The sensor has the same dimension as mentioned in the section *5.4.1*. Two different measurements were performed, one only with air filled sensor within the sensing zone and the other with the sensor completely filled with water. Each measurement cycle consists of 66 independent capacitance measurements. Figure 5.39 and 5.40 illustrates the simulated versus experimental measured capacitances for all the cases from $C_{1\text{-}2}$ to $C_{11\text{-}12}$.

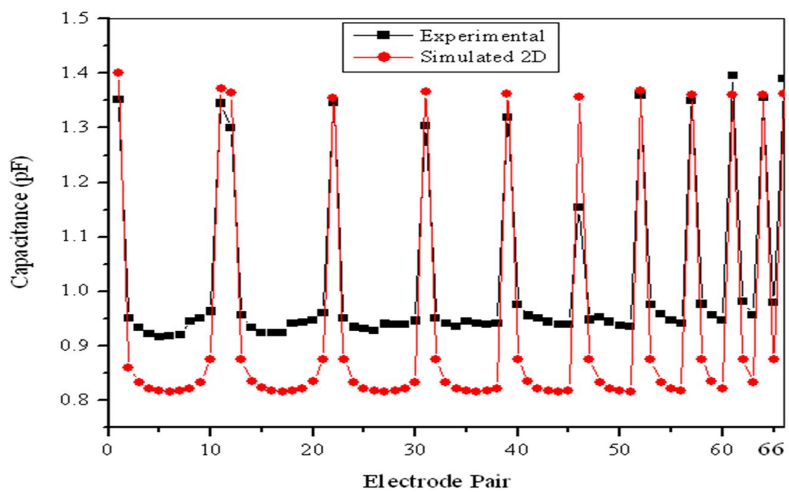

Figure 5.39: Simulated Capacitances for Air Filled Sensor from 2D Case and Capacitances Found From Real Experimental Measurements.

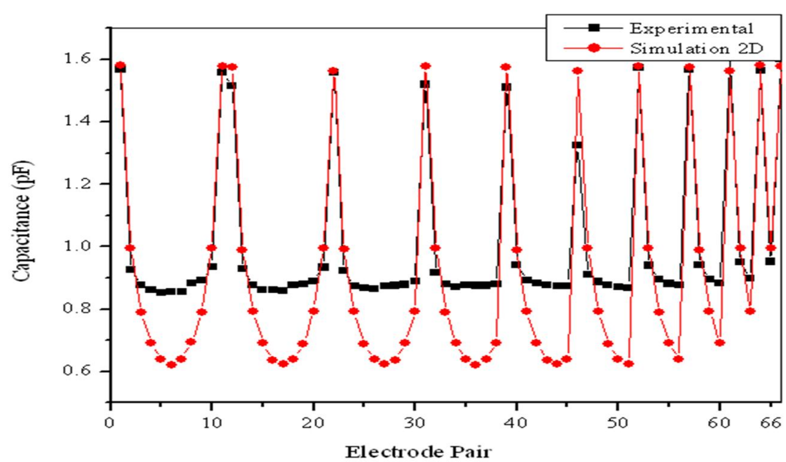

Figure 5.40: Simulated Capacitances for Water Filled Sensor from 2D Case and Capacitances Found From Real Experimental Measurements.

Figure 5.41 (a) and (b) demonstrates the relative errors for the two cases over the whole frame of 66 capacitance measurements. These plots show that the accuracy for 2D model is within 15-25%. This error difference in percentage is mainly because of the reasons like;

i. Errors in the modelled geometry can cause some minor geometrical differences between physical and simulated sensor.

ii. The difference in the modelled and real permittivity/conductivity in the ECT pipe.

iii. External interferences such as; signal-to-noise ratio.

iv. Instrumental/Systematic errors; the capacitance measurement system is highly sensitive and hence, change in capacitance can be measured with great accuracy. However, the systematic errors of these instruments can be excluded as an error source.

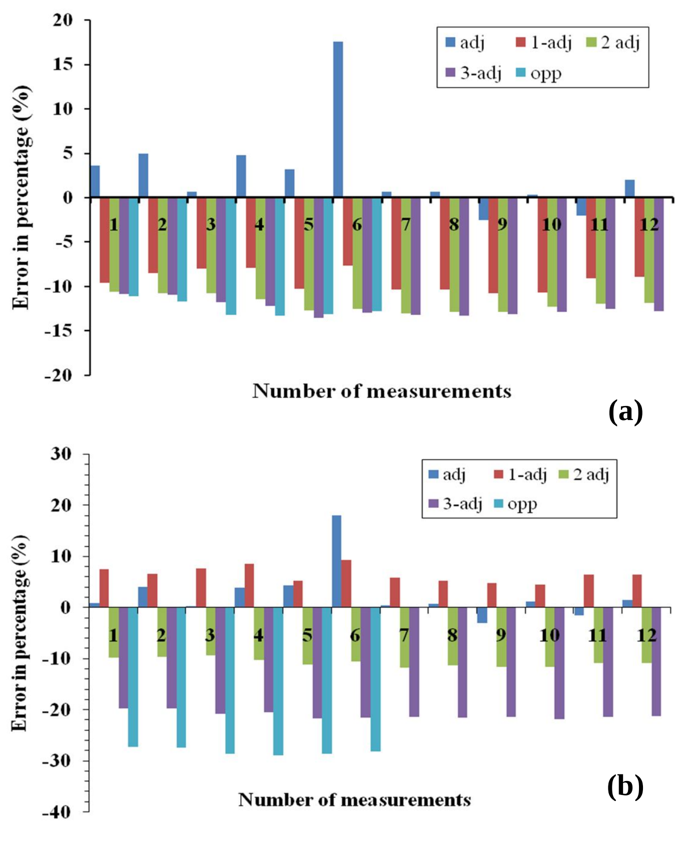

Figure 5.41: Relative Error in Percentage for (a) Empty Sensor and (b) Full Sensor.

5.11 Summary

In this chapter, three kinds of bubble flow regimes were examined and analysed by using the visual observation technique. Bubble flow regime map have also been established based on the experimental data for the vertical co-current bubble column in a 49.3 mm inner diameter. This is in good agreement with the previous studies considering the differences in the experimental conditions.

Bubbles characteristics exhibit different dependencies on gas and liquid superficial velocities in different flow regimes. Therefore, it is important to keep the flow regime in mind when undertaking further study of hydrodynamics. This study includes the estimation of bubble size by using the photographic technique and statistical analysis. Based on this observation it was found that there is a reduction in bubble diameter with increase in superficial gas velocity and this also agreed with some correlations proposed by previous researchers using approximately the same experimental conditions.

Electrical Capacitance Tomography (ECT) was applied on the experimental setup not only for the estimation of void fraction but also to obtain the tomographic images for air-water flows. The tomographic images obtained showed good agreement with the theoretical predictions and with what could be observed through the transparent section of the flow loop. The ECT sensor was calibrated using adaptive calibration method for permittivity contrast between 1 and 80. The 12 electrode ECT sensor was also simulated using the COMSOL Multiphysics Software in order to theoretically estimate the capacitance of the ECT sensor. The 2D simulation results were compared to the experimental data and found to be in good agreement to each other with an error percentage in between 15-25%. This provides confidence in the experimental findings.

The application of ECT for void fraction calculation was done by using the distribution models and image/pixel analysis. For the analysis of raw data obtained from the ECT system the application of distribution models result in analysing the normalised and measured capacitance values for 12 electrode measurements. By using these models, the normalised capacitance values for this experimental condition were found to be in the range of $0.6 \geq C_n \geq 0.7$. However, the permissible range for normalised values of capacitances lies between 0 and 1. The overall void fraction was also calculated from normalised pixel values in the reconstructed ECT image.

The void fraction was also determined by using differential pressure measurements. It was applied as a reference measurement because it's the most simple in operation, non-intrusive and economical method that has been applied by various researchers to compare the void fraction measurements by some other methods. On the application of differential pressure (ΔP) method on the vertical co-current bubble column, it was found that the void fraction increases linearly on increasing the superficial gas velocity which shows a good agreement with other studies.

Keeping in view the practical importance of drift-flux model for two-phase bubble flow analysis, this study has also used precedent researcher values of drift-flux model to compare with the current experimental results. Furthermore, the comparison between the experimental and measured data of void fraction shows an average percentage deviation of ± 20%.

The significant finding of this study has also discussed in this chapter in terms of comparison between the void fraction measurements using ECT, Delta-P and Photographic techniques. It has been found from the analysis that the measurements generally follow the increasing trend of void fraction with an increase in air flow rates.